

---

**RESEARCH ARTICLE**

# Key parameters for droplet evaporation and mixing at the cloud edge

J. Fries<sup>1</sup> | G. Sardina<sup>2</sup> | G. Svensson<sup>3</sup> | B. Mehlig<sup>1</sup>

<sup>1</sup>Department of Physics, Gothenburg University, SE-41296 Gothenburg, Sweden

<sup>2</sup>Department of Mechanics and Maritime Sciences, Division of Fluid Dynamics, Chalmers University of Technology, SE-41296 Gothenburg, Sweden

<sup>3</sup>Department of Meteorology, Stockholm University and Swedish e-science Research Centre, Stockholm, Sweden

## Correspondence

Bernhard Mehlig, Department of Physics, Gothenburg University, SE-41296 Gothenburg, Sweden  
Email: bernhard.mehlig@physics.gu.se

## Funding information

Vetenskapsrådet, grant number: 2017-3865; Formas, grant number: 2014-585; Knut and Alice Wallenberg Foundation, Dnr. KAW 2014.0048

The distribution of liquid water in ice-free clouds determines their radiative properties, a significant source of uncertainty in weather and climate models. Evaporation and turbulent mixing cause a cloud to display large variations in droplet-number density, but quite small variations in droplet size (Beals et al., 2015). Yet direct numerical simulations of the joint effect of evaporation and mixing near the cloud edge predict quite different behaviors, and it remains an open question how to reconcile these results with the experimental findings. To infer the history of mixing and evaporation from observational snapshots of droplets in clouds is challenging because clouds are transient systems. We formulated a statistical model that provides a reliable description of the evaporation-mixing process as seen in direct numerical simulations, and allows to infer important aspects of the history of observed droplet populations, highlighting the key mechanisms at work, and explaining the differences between observations and simulations.

## KEYWORDS

cloud micro-physics, turbulent mixing, droplet evaporation, Lagrangian droplet dynamics

# 1 | INTRODUCTION

Clouds play a major role in regulating weather and climate on Earth, by modulating the incoming solar radiation. Despite substantial scientific advances in the last decades, clouds still represent the primary source of uncertainty in climate projections (Pincus et al., 2018; Stocker et al., 2013). A key challenge is to understand how entrainment of dry air at the edges of ice-free clouds affects the size distribution and number density of droplets (Blyth, 1993). This is important because amount and distribution of liquid water determine cloud optical properties (Kokhanovsky, 2004) and precipitation efficiency (Burnet and Brenguier, 2007). As a consequence, weather and climate models are sensitive to how entrainment at the cloud edge is parameterised (Mauritsen et al., 2012).

The optical properties of clouds are of crucial importance for the radiation balance of the Earth's climate system (Caldwell et al., 2016; Dufresne and Bony, 2008). The size distribution and number density of droplets are key ingredients, because the light-extinction coefficient of the cloud is determined by the number of the droplets it contains, times their average surface area (Kokhanovsky, 2004).

Regarding precipitation efficiency, the mechanism of rain formation in ice-free clouds is a longstanding unresolved problem in atmospheric physics (Grabowski and Wang, 2013). A broad initial droplet-size distribution is needed to activate the collisions and coalescences of droplets that are necessary for the rapid onset of rain formation observed empirically in warm clouds (Devenish et al., 2012; Szumowski et al., 1997, 1998). Microscopic droplets grow by condensation of water vapour, or shrink by evaporation. Yet when a droplet-containing parcel does not mix with its surroundings, condensation causes the droplet-size distribution to narrow because the diffusional growth of a droplet is inversely proportional to its radius, so that small droplets grow faster than large ones (Rogers and Yau, 1989).

Turbulence has a strong influence upon droplet condensation and evaporation in clouds (Bodenschatz et al., 2010). Turbulent mixing causes water-vapour and liquid-water content to fluctuate on different length and time scales (Vailancourt et al., 2001). As a consequence, nearby droplets may have experienced quite different growth histories. The droplets of a cloudy parcel that is mixed with dry air evaporate at different rates, so that the droplet-size distribution broadens (Lanotte et al., 2009; Sardina et al., 2015, 2018; Li et al., 2020). Cloud-resolving simulations (Hoffmann and Feingold, 2019) show that this mechanism can have a strong effect on droplet-number densities in turbulent clouds.

Entrainment of dry air at the cloud edge triggers rapid changes in the droplet-size distribution (Perrin and Jonker, 2015; Abade et al., 2018). As turbulence mixes dry air into the cloud it creates long-lasting regions of dry air where droplets can rapidly evaporate. Droplets in regions with higher water-vapour concentration, by contrast, may saturate the air and survive for a much longer time, Figure 1(a). While droplets evaporate turbulence mixes the cloud at many length scales, ranging from the Kolomogorov length – of the order of millimetres (Devenish et al., 2012) – to a few kilometres (Rogers and Yau, 1989). Evaporation and mixing on a spatial scale  $\ell$  depend on the turbulent mixing time  $\tau_\ell$  at that scale, and upon the relevant thermodynamic time scale  $\tau$ . Their ratio forms a Damköhler number  $Da = \tau_\ell / \tau$  (Dimotakis, 2005). The thermodynamic process parameterised by  $Da$  is limited by the rate of mixing if  $Da$  is large, and limited by thermodynamics if  $Da$  is small. The dynamics at large Damköhler numbers is referred to as inhomogeneous mixing (Baker et al., 1980), where some droplets evaporate completely while others do not evaporate at all. Small- $Da$  mixing is called homogeneous, where droplets evaporate at approximately the same rate, so that the droplet-size distribution remains narrow.

The notion of homogeneous and inhomogeneous mixing remains debated (Tölle and Krueger, 2014), but it can be given a precise meaning in terms of the fraction  $P_e(t)$  of droplets that have completely evaporated at time  $t$ . However, it is at present not understood which mechanisms and parameters that determine the transition from homogeneous to inhomogeneous mixing. Several authors have attempted to describe turbulent mixing in terms of one Damköhler number. Lehmann et al. (2009) used a combined microphysical response time  $\tau_r$ , a function of the two thermodynamic

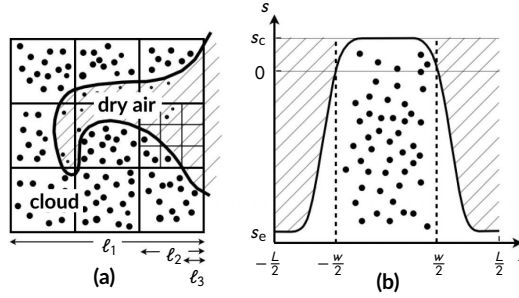


FIGURE 1 (a) Effect of mixing on local droplet populations (schematic). On large spatial scales ( $\ell_1$  and  $\ell_2$ ) mixing and evaporation is not yet complete, but some smaller regions (of size  $\ell_3$ ) are in local steady states: saturated air with droplets, or subsaturated air without droplets. (b) Initial cloud configuration in our model. Before mixing, moist air and droplets reside in a  $w \times L \times L$  slab, contained in a cubic domain of side length  $L$ . Regions with dry air are dashed. The solid line is the initial profile of supersaturation  $s$  (see text).

time scales of the problem,  $\tau_d$  (droplet evaporation) and  $\tau_s$  (supersaturation relaxation). Lu et al. (2018), by contrast, suggest that  $\tau_d$  should be used to formulate a single-parameter criterion for inhomogeneous mixing. The direct numerical simulations (DNS) by Kumar et al. (2018) explored how the nature of mixing changes as  $\tau_L/\tau_r$  increases with the linear size  $L$  of the simulated domain. However, no clear sign of inhomogeneous mixing was found. The authors mention that this may be a consequence of the thermodynamic setup used. Another possibility is that the simulated system was just not large enough. Jeffery (2007) emphasised that evaporation and mixing cannot be described by a single  $Da$  alone, because there are two thermodynamic time scales, leading to three key non-dimensional parameters,  $Da_d$ ,  $Da_s$ , and the volume fraction  $\chi$  of cloudy air. However, Jeffery only studied the case  $Da_d = Da_s$  and did not discuss the implications of varying the Damköhler numbers separately. Pinsky et al. (2016a) and Pinsky and Khain (2018a) modified an equation for advected liquid water (Rogers and Yau, 1989) into a diffusion-reaction equation for the droplet-size distribution, and emphasised the significance of a non-dimensional parameter, their potential evaporation parameter.

Here we derive a statistical model for evaporation and turbulent mixing at the cloud edge from first principles. The model takes into account the multi-scale turbulent dynamics, as turbulent clouds can have large Reynolds numbers;  $Re \sim 10^7$  is a conservative estimate for convective clouds (Devenish et al., 2012). The model quantitatively predicts the outcomes of the DNS by Kumar et al. (2012, 2013, 2014, 2018). Furthermore, the model shows in accordance with Jeffery (2007) that the evolution of the droplet-size distribution is determined by  $Da_d$ ,  $Da_s$ , and  $\chi$ . We find that the potential evaporation parameter of Pinsky et al. (2016a) and Pinsky and Khain (2018a) is simply determined by the ratio of the Damköhler numbers. Finally, the model allows to interpret the results of in-situ measurements of clouds at the centimetre scale (Beals et al., 2015).

## 2 | METHOD

We study mixing and evaporation of cloud droplets by mixing moist air, droplets, and dry air in a cubic domain of side length  $L$  with periodic boundary conditions. Initially, the saturated or slightly supersaturated moist air with supersaturation  $s_c \geq 0$  is contained in a  $w \times L \times L$  slab together with  $N_0$  randomly distributed water droplets, Figure 1(b).

The dry air, initially outside the slab, has negative supersaturation  $s_e < 0$ . The mixing is driven by statistically stationary homogeneous isotropic turbulence, with turbulent kinetic energy TKE and mean dissipation rate per unit mass  $\varepsilon$  (Frisch, 1995). Essentially the same setup is used in the DNS of Kumar et al. (2012, 2013, 2014, 2018), which allows us to understand their simulation results in terms of our model.

## 2.1 | Microscopic equations

For the turbulent mixing, we start from the microscopic equations of Kumar et al. (2018) and earlier studies (Vaillancourt et al., 2002; Paoli and Shariff, 2009; Lanotte et al., 2009; Kumar et al., 2014; Perrin and Jonker, 2015). We neglect buoyancy, particle inertia and settling, temperature changes due to vertical motion, temperature and pressure dependencies of the thermodynamic coefficients, and subsume the joint effects of temperature and water vapour into a single supersaturation field.

We denote fluid velocity and pressure by  $\mathbf{u}(\mathbf{x}, t)$  and  $p(\mathbf{x}, t)$ , and supersaturation by  $s(\mathbf{x}, t)$ . The spatial position of droplet  $\alpha$  is  $\mathbf{x}_\alpha(t)$ , its radius equals  $r_\alpha(t)$ , and the index  $\alpha$  ranges from 1 to  $N_0$ . We non-dimensionalise as follows:  $\mathbf{u}' = \mathbf{u}/U$ ,  $\mathbf{x}' = \mathbf{x}/(U\tau_L)$ ,  $t' = t/\tau_L$ ,  $p' = p/(\varrho_a U^2)$ ,  $\mathbf{x}'_\alpha = \mathbf{x}_\alpha/(U\tau_L)$ ,  $s' = s/|s_e|$ ,  $r'_\alpha = r_\alpha/r_0$ , and  $s'_c = s_c/|s_e|$ . Here  $U = \sqrt{2\text{TKE}/3}$  is the turbulent r.m.s. velocity,  $\tau_L = \text{TKE}/\varepsilon$  is the large-eddy time [ $\propto L/U$  if the size of the largest eddies is of the order  $L$  (Pope, 2000)],  $\varrho_a$  is the reference mass density of air,  $r_0 = [N_0^{-1} \sum_{\alpha=1}^{N_0} r_\alpha(0)^3]^{1/3}$  is the initial volume-averaged droplet radius, and  $|s_e|$  is the (positive) subsaturation of the air outside the initial cloud slab. Dropping the primes, the microscopic equations take the non-dimensional form:

$$\frac{D}{Dt} \mathbf{u} = -\nabla p + \text{Re}_L^{-1} \nabla^2 \mathbf{u} \quad \text{with} \quad \nabla \cdot \mathbf{u} = 0, \quad (1a)$$

$$\frac{D}{Dt} s = (\text{Re}_L \text{Sc})^{-1} \nabla^2 s - \text{Da}_s \chi V \overline{r_\alpha(t) s(\mathbf{x}_\alpha, t)}, \quad (1b)$$

$$\frac{d}{dt} \mathbf{x}_\alpha = \mathbf{u}(\mathbf{x}_\alpha, t), \quad (1c)$$

$$\frac{d}{dt} r_\alpha = \text{Da}_d s(\mathbf{x}_\alpha(t), t) / (2r_\alpha) \quad \text{if } r_\alpha > 0. \quad (1d)$$

Equations 1a are the incompressible Navier-Stokes equations, with Lagrangian time derivative  $\frac{D}{Dt} = \partial_t + (\mathbf{u} \cdot \nabla)$ . In DNS of Equations 1, a forcing is imposed to sustain stationary turbulence. This is not necessary in the model introduced below, and we therefore do not include a forcing term in Equation 1a. Equation 1b is the equation for supersaturation. The first term on its r.h.s. describes diffusion of the supersaturation  $s(\mathbf{x}, t)$ . The second term models the effect of condensation and evaporation through the average  $\overline{r_\alpha(t) s(\mathbf{x}_\alpha, t)}$ , taken over all droplets in the vicinity of  $\mathbf{x}$ . Droplets are advected by the turbulent flow (Equation 1c), and Equation 1d models how the droplet radius  $r_\alpha$  changes due to evaporation and condensation. When a droplet has evaporated completely, we impose that it must remain at  $r_\alpha = 0$ . In the derivation of Equation 1d,  $s(\mathbf{x}_\alpha(t), t)$  enters as the supersaturation at distances from the droplet that are much larger than the droplets radius (Rogers and Yau, 1989). In other words, Equation 1d relies on a scale separation between droplet sizes and lengths that characterise supersaturation fluctuations generated by turbulent mixing (Vaillancourt et al., 2001). As a consequence, droplets interact locally with the supersaturation field over finite volumes through the average  $\overline{r_\alpha(t) s(\mathbf{x}_\alpha, t)}$  in Equation 1b. Further details regarding Equations 1 are given in the Supporting Information (SI), where we also show how to derive Equations 1 from the more detailed dynamical description of Vaillancourt et al. (2001, 2002), Kumar et al. (2014, 2018), and Perrin and Jonker (2015).

An advantage of writing the dynamics in non-dimensional form is that this determines the independent non-dimensional parameters. First,  $\text{Re}_L = \frac{2}{3} \text{TKE}^2 / (\varepsilon \nu)$  is the turbulence Reynolds number (Pope, 2000),  $\nu$  is the kinematic viscosity of air. The Schmidt number is defined as  $\text{Sc} = \nu/\kappa$ , where  $\kappa$  is the diffusivity of  $s$ . The volume fraction of

cloudy air is given by  $\chi = w/L$ , and  $V = [L/(U\tau_L)]^3$  is the dimensionless domain volume. The Damköhler number  $Da_s$  is defined as  $Da_s = \tau_L/\tau_s$ , where  $\tau_s = (4\pi A_2 A_3 \rho_w n_0 r_0)^{-1}$  is the supersaturation relaxation time. This is the time scale at which the supersaturation decays towards saturation, assuming that all droplets have the same radius  $r_0$ , and for droplet number density  $n_0 = N_0/(wL^2)$ . Further,  $\rho_w$  is the density of pure liquid water, and  $A_2$  and  $A_3$  are thermodynamic coefficients, specified in the SI. The Damköhler number  $Da_d$  is defined as  $Da_d = \tau_L/\tau_d$ , where  $\tau_d = r_0^2/(2A_3 |s_e|)$  is the droplet evaporation time, the time that it takes for a droplet of radius  $r_0$  to evaporate completely in a constant ambient supersaturation  $s_e < 0$ .

The Damköhler numbers determine the extent to which saturation and droplet evaporation are limited by the rate of mixing (Dimotakis, 2005). Saturation is mixing limited at large  $Da_s$ , since regions with evaporating droplets – created by mixing of cloudy and dry air at the time scale  $\tau_L$  – saturate faster than  $\tau_L$ . When  $Da_s$  is small, by contrast, evaporating droplets saturate the air more slowly than it is mixed. In this case, saturation is not limited by the rate of mixing. Droplet evaporation is mixing limited at large  $Da_d$ , since droplets then evaporate more rapidly than the exposure to subsaturated air changes. At small  $Da_d$ , mixing is faster than droplet evaporation, and droplets tend to evaporate mainly after the system has been mixed. The droplets then experience roughly the same supersaturation as they evaporate.

In the limit  $Re_L \rightarrow \infty$ , three key non-dimensional parameters remain in Equations 1:  $\chi$ ,  $Da_d$ , and  $Da_s$ . The system can be parameterised by  $\chi$ ,  $Da_d$ , and

$$\mathcal{R} = Da_d/Da_s. \quad (2)$$

In this way, the scale dependence of the mixing process is contained in  $Da_d$  only. The Damköhler-number ratio  $\mathcal{R}$  is inversely proportional to the density of liquid water in the cloud slab; it regulates the moisture of the mixing process (details in SI). The bifurcation between moist steady states, where droplets remain in saturated air, and dry steady states, where all droplets have evaporated completely (Jeffery, 2007; Kumar et al., 2013; Pinsky et al., 2016b), occurs at a critical value of  $\mathcal{R}$ ,  $\mathcal{R}_c$ . The critical ratio  $\mathcal{R}_c$  can be computed from the conserved quantity  $\theta = -\langle s(t) \rangle - \frac{2\chi}{3\mathcal{R}} [1 - P_e(t)] \langle r^3(t) \rangle$ , which is analogous to the liquid-water potential temperature at fixed altitude (Gerber et al., 2008; Lamb and Verlinde, 2011; Kumar et al., 2014). Here,  $P_e(t)$  is the fraction of completely evaporated droplets, the fraction of droplets for which  $r_\alpha(t) = 0$  at time  $t$ . Furthermore,  $\langle s(t) \rangle = V^{-1} \int_V s(\mathbf{x}, t) d\mathbf{x}$  is the volume average of supersaturation, and  $\langle r^3(t) \rangle = \{[1 - P_e(t)]N_0\}^{-1} \sum_{\alpha=1}^{N_0} r_\alpha(t)^3$  is the mean cubed droplet radius conditioned on  $r_\alpha(t) > 0$  by the factor  $[1 - P_e(t)]^{-1}$ . The conservation of  $\theta$  can be concluded by integrating Equation 1b for supersaturation over the domain volume, see the SI for details. Moist steady states have  $\langle r^3(t) \rangle > 0$  and  $\langle s(t) \rangle = 0$ , dry steady states have  $P_e(t) = 1$  and  $\langle s(t) \rangle < 0$ , so the sign of  $\theta$  determines whether the steady-state is moist or dry. The value of  $\theta$  is determined by the initial conditions,  $\theta = -\langle s(0) \rangle - 2\chi/(3\mathcal{R})$ . Setting  $\theta = 0$ , we find the critical Damköhler-number ratio  $\mathcal{R}_c = -\frac{2}{3}\chi/\langle s(0) \rangle$ .

DNS of Equations 1 for experimentally observed dissipation rates and droplet-number densities are feasible only for quite small systems (Kumar et al., 2018). This restricts the range of scales that can be explored, and makes it difficult to detect inhomogeneous mixing in DNS. We therefore pursue an alternative approach and adapt a PDF model (Pope, 2000) – commonly used to describe combustion processes (Haworth, 2010) – to the inhomogeneous cloud edge. As opposed to the kinematic statistical models reviewed by Gustavsson and Mehlig (2016), we must also take thermodynamic processes into account.

## 2.2 | Statistical model

Statistical models have been used to describe droplets in a supersaturation field that fluctuates around zero, as in the cloud core (Paoli and Shariff, 2009; Sardina et al., 2015; Chandrakar et al., 2016; Siewert et al., 2017). At the cloud edge, there are large deviations from this equilibrium. Jeffery (2007), Pinsky et al. (2016a), and Pinsky and Khain (2018a) formulated models for the cloud edge where droplets evaporate in direct response to a mean supersaturation field. This does not take into account that mixing is local, and that small droplets are advected together with the supersaturation field. For an accurate description of mixing and evaporation, it is essential to describe how each droplet carries its own local supersaturation (Siewert et al., 2017). Our model does just that. It is derived from first principles using the established framework of PDF models (Pope, 2000).

For the configuration shown in Figure 1(b) we derive one-dimensional statistical-model equations from Equations 1 (details in the SI):

$$du = -\frac{3}{4}C_0 u dt + \left(\frac{3}{2}C_0\right)^{1/2} d\eta, \quad (3a)$$

$$\frac{d}{dt}s = -\frac{1}{2}C_\phi [s - \langle s(x, t) \rangle] - Da_s \chi V \langle r(t)s(x, t) \rangle, \quad (3b)$$

$$\frac{d}{dt}x = u, \quad (3c)$$

$$\frac{d}{dt}r = Da_d s / (2r) \quad \text{if } r > 0. \quad (3d)$$

Equation 3a describes the fluctuating acceleration of Lagrangian fluid elements in turbulence. Here,  $d\eta$  are Brownian increments with zero mean and variance  $dt$ , and  $C_0$  is an empirical constant (Pope, 2011). Each Lagrangian fluid element has a supersaturation  $s$ , and may contain a droplet (at position  $x$ , of size  $r$ ). Equation 3b approximates the supersaturation dynamics as decay towards  $\langle s(x, t) \rangle$ , regulated by the empirical constant  $C_\phi$  (Pope, 2000). The second term on the r.h.s. of Equation 3b represents the effect of condensation and evaporation through  $\langle r(t)s(x, t) \rangle$ . The position-dependent averages  $\langle \cdots \rangle$  in Equation 3b are taken over fluid elements located at  $x$  at time  $t$  (details in the SI). The statistical-model Equations 3 becomes independent of  $Re_L$  at large Reynolds numbers, where  $C_0$  approaches a definite limit (Pope, 2011). It is independent of  $Sc$ , in accordance with the known behaviour of advected scalars in fully developed turbulence (Shraiman and Siggia, 2000).

Equations 3 rest upon a probabilistic description of the dynamics of the two phases, droplets and air (Pope, 2000; Jenny et al., 2012). The corresponding evolution equations, dictated by Equations 1, contain unclosed terms that must be approximated (Pope, 1985; Haworth, 2010) to obtain a closed model such as Equations 3. Following Pope (2000), we cast the model into the form of stochastic dynamical equations for Lagrangian fluid elements. Since the dynamics is statistically one-dimensional in our configuration, we can average over the  $y$  and  $z$  coordinates to obtain Equations 3 in one-dimensional form. For the closures, we rely on standard approximations, common and justified in PDF modeling of single-phase flows (Pope, 1985), and in models for turbulent combustion (Haworth, 2010; Jenny et al., 2012; Stöllinger et al., 2013). The explicit mathematical approximations for the closures provided in the SI render the interpretation of the statistical model definite, and indicate how to improve the model when necessary.

In the following, we briefly summarise the closures. Equation 3a contains the closure for fluid-element accelerations. It reproduces the empirically observed effect of turbulent diffusion of passive-scalar averages (Pope, 2000). Equation 3b contains two closure approximations. First, the decay towards  $\langle s(x, t) \rangle$  approximates the diffusion of supersaturation. This closure ensures that the mean of a passive scalar is conserved, and that a passive scalar remains bounded between its minimal and maximal values (Pope, 2000). Furthermore, it describes the decay of passive-scalar variance in statistically homogeneous turbulent mixing of two scalar concentrations (Pope, 2000). However, this closure does not reproduce the relaxation of the single-point PDF of scalar concentration – from a two-peaked distri-

TABLE 1 Summary of statistical-model simulations, details in SI. Damköhler numbers  $Da_d$  and  $Da_s$ , Damköhler-number ratio  $\mathcal{R}$ , critical ratio  $\mathcal{R}_c$ , and volume fraction  $\chi$  of cloudy air

Simulation	$Da_d$	$Da_s$	$\mathcal{R}$	$\mathcal{R}_c$	$\chi$
Figure 2 and 3(a) [dry]	2.44	0.968	2.52	0.859	0.428
Figure 2 [moist]	1.09	1.43	0.76	0.859	0.428
Figure 3(b) [very moist]	0.754	8.20	0.092	0.683	0.4
Figure 4	$5E^{-3}$ - $4E^2$	$1E^{-3}$ - $9E^3$	$4E^{-2}$ - $4E^0$	0.913	0.429
Figure 5(a)	$1E^{-2}$ - $1E^3$	$6E^{-2}$ - $6E^3$	0.17	0.18-2.7	0.2-0.8
Figure 5(b)	$1E^{-2}$ - $8E^2$	$3E^{-3}$ - $4E^4$	$2.4E^{-2}$ - $2.9E^{-2}$	0.38-0.41	0.369-0.374

bution via a U-shaped distribution into a Gaussian (Eswaran and Pope, 1988; Pope, 1991). For our initial conditions [Figure 1(b)], the decay towards  $\langle s(x, t) \rangle$  captures the supersaturation fluctuations experienced by a fluid element as it moves towards or away from the most cloudy region. Note that this closure does not account for large saturated cloud structures that tend to relax slowly towards  $\langle s(x, t) \rangle$ . Such events are most relevant during the initial stages of the mixing-evaporation process, and their effect is expected to diminish with time, as large cloud structures are mixed into smaller and smaller structures. Consequently, the statistical model may describe short initial transients only qualitatively, not quantitatively.

The second closure in Equation 3b approximates the effects of droplet phase change on the supersaturation field: the local average  $\overline{r_\alpha(t)s(\mathbf{x}_\alpha, t)}$  in Equation 1b is replaced by the ensemble average  $\langle r(t)s(x, t) \rangle$ . This is the simplest closure that preserves the conservation of the parameter  $\theta$ , and it is therefore common in PDF models that describe combustion of particles in turbulence (Haworth, 2010; Jenny et al., 2012; Stöllinger et al., 2013). The average  $\langle r(t)s(x, t) \rangle$  takes into account that droplet evaporation is delayed locally when nearby droplets saturate the surrounding air. Since we obtain closure by replacing the local average  $\overline{r_\alpha(t)s(\mathbf{x}_\alpha, t)}$  by an average over fluid elements with one-dimensional dynamics, variations in the rate of supersaturation relaxation in the  $y$  and  $z$ -coordinates are not described.

It is expected that the large cloud structures mentioned above, and their three-dimensional forms, matter more at very large Damköhler numbers. Therefore it cannot be excluded that the statistical model is only qualitative in this extreme limit. Below we show that the model works very well even for the largest Damköhler numbers in DNS studies Kumar et al. (2012, 2014). Also, since the statistical model is derived using the established framework of PDF models (Pope, 2000), it can be straightforwardly improved by incorporating additional variables in the probabilistic description (Pope and Chen, 1990; Pope, 2000; Meyer and Jenny, 2008), or by using more refined approximations (Pope, 1991; Jenny et al., 2012).

## 3 | RESULTS

### 3.1 | Comparison with DNS

The statistical model can be used to understand DNS results of Kumar et al. (2012, 2013, 2014, 2018). Figure 2 shows good agreement for the time evolution of the fraction  $P_e(t)$  of droplets that have completely evaporated, even though the statistical-model dynamics is slightly slower. Panels (a) and (b) in Figure 3 show that the model reproduces the

TABLE 2 Parameters of DNS shown in Figure 4: Damköhler number  $Da_d$ , Damköhler-number ratio  $\mathcal{R}$ , critical ratio  $\mathcal{R}_c$ , and volume fraction  $\chi$  of cloudy air. Some dimensional parameters are also shown: domain size  $L$ , mean dissipation rate  $\varepsilon$ , and droplet-number density  $n_0$  of the initially cloudy air.

Reference	Non-dimensional parameters					Dimensional parameters		
	$Da_d$	$Da_s$	$\mathcal{R}$	$\mathcal{R}_c$	$\chi$	$L$ [cm]	$\varepsilon$ [cm <sup>2</sup> /s <sup>3</sup> ]	$n_0$ [cm <sup>-3</sup> ]
◦ Andrejczuk et al. (2006)	$8E^{-1}$ - $1E^2$	$3E^0$ - $3E^2$	0.13-2.8	0.10-4.5	0.13-0.87	64	$4E^{-1}$ - $9E^2$	$1E^2$ - $1E^3$
△ Kumar et al. (2012)	$8E^{-3}$ - $8E^{-1}$	$8E^{-2}$ - $8E^0$	$9.2E^{-2}$	0.68	0.4	26	34	164
□ Kumar et al. (2013)	0.14, 0.31	0.62, 0.41	0.22, 0.73	0.68	0.4	26	34	164
◇ Kumar et al. (2014)	0.61-2.4	0.97-1.9	0.31-2.5	0.84	0.42	51	34	153
▽ Kumar et al. (2018)	0.12-0.91	0.51-4.0	0.23	0.90-0.95	0.42-0.45	$1E^1$ - $2E^2$	32-35	120

broadening of the droplet-size distribution. The slightly slower dynamics in Figure 2 and the deviations in the tails in Figure 3 suggest that the statistical model does not reproduce the most rapid evaporation rates. This could be due to turbulent fluctuations in the supersaturation diffusion, neglected in Equation 3b. Kumar et al. (2012, 2014) compute droplet-size distributions with prominent exponential tails using DNS – some of them are seen in Figure 3 (black lines) – and connect these tails to corresponding exponential tails in the PDF of supersaturation at droplet positions. In our statistical-model simulations we observe heavy tails in the PDF of supersaturation at the droplet position, but the tails are less pronounced than in the DNS (not shown). Heavy tails are consistent with the results of Eswaran and Pope (1988) mentioned above, who observed how an initially bimodal supersaturation relaxes.

Despite these shortcomings, our model describes the time evolution of  $P_e(t)$  very well (Figure 2). It is also a significant improvement over models in which the droplets interact with a mean supersaturation field (Jeffery, 2007; Pinsky et al., 2016a; Pinsky and Khain, 2018a). In reality, the droplets react to the local supersaturation, as mentioned above, and this may be particularly important at large values of  $Da_d$ , where locally saturated regions can persist for a long time.

Figure 4 shows the steady-state value  $P_e^*$  of  $P_e(t)$  computed from the statistical model as a function of  $Da_d$  and  $\mathcal{R}/\mathcal{R}_c$ . We see how  $P_e^*$  increases with both  $Da_d$  and  $\mathcal{R}/\mathcal{R}_c$ . The DNS results of Andrejczuk et al. (2006) and Kumar et al. (2012, 2013, 2014, 2018) form a pattern in Figure 4 that verifies these dependencies: open symbols correspond to DNS with little or no complete evaporation in the steady state ( $P_e^* < 10\%$ ), and filled symbols to  $P_e^* > 10\%$ . Figure 4 also explains why the DNS of Kumar et al. (2018) did not exhibit significant levels of inhomogeneous mixing: since their  $\mathcal{R}$  was quite small, small values of  $P_e^*$  require values of  $Da_d$  much larger than unity ( $Da_d \sim 10^2$  for  $P_e^* = 10\%$ ). Furthermore, the substantially different outcomes of the DNS of Kumar et al. (2012) and Kumar et al. (2014) are explained, their parameters lie on opposite sides of the bifurcation line. Figure 4 also explains, at least qualitatively, numerical results of DNS of transient turbulence with quite different initial conditions (Andrejczuk et al., 2006), namely how the amount of complete droplet evaporation increases with both  $\mathcal{R}/\mathcal{R}_c$  and  $Da_d$ . There is no parameter corresponding directly to  $Da_d$  in the simulations of Andrejczuk et al. (2006), because they are for different initial conditions and flows. We therefore place these simulations in Figure 4 by computing a time-scale ratio that, in a qualitative sense, incorporates the same physics as  $Da_d$  (details in the SI). Key parameters of the DNS in Figure 4 are summarised in Table 2, a complete description is provided in the SI.



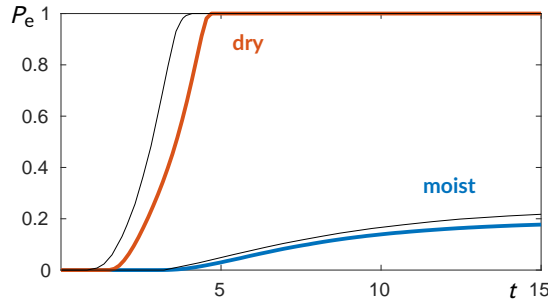


FIGURE 2 Fraction  $P_e(t)$  of droplets that have completely evaporated as a function of non-dimensional time  $t$ , parameters in Table 1. Coloured lines are statistical-model simulations, black lines are DNS of Kumar et al. (2014).

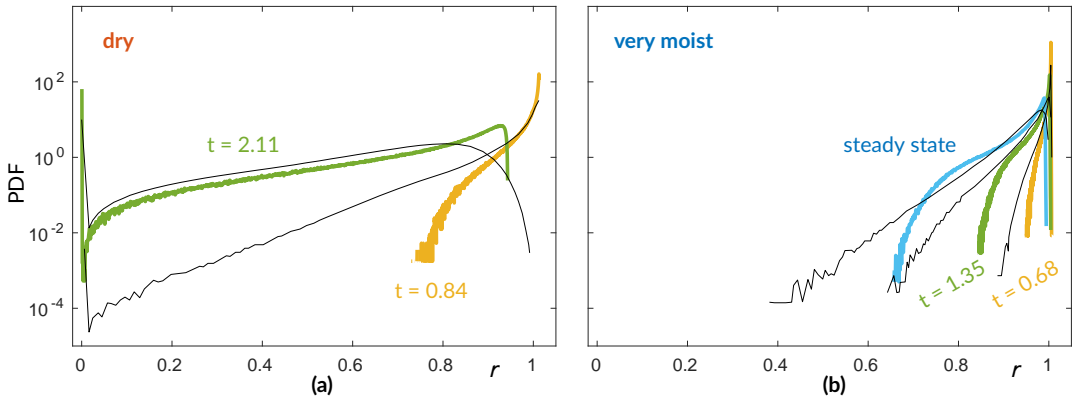


FIGURE 3 (a) Evolution of the droplet-size distribution (parameters in Table 1) for different times. The probability density of the non-dimensional droplet radius  $r$  is shown for the statistical-model (coloured lines) and DNS of Kumar et al. (2014) (black lines). The initial droplet-size distribution is monodisperse, and centred at  $r = 1$ . (c) Same as (b), but for a very moist case (parameters in Table 1) and DNS of Kumar et al. (2012).

### 3.2 | Mixing histories from observations

A common way of characterising the droplet content of a cloud is to plot the mean cubed radius  $r^3$  and number density  $n$  of droplets for observed cloud-droplet populations in a mixing diagram. Figure 5(a) shows a mixing diagram with empirical data from Beals et al. (2015). Black crosses are values of  $r^3$  and  $n$  extracted from snapshots (linear size 15 cm) of local droplet populations measured during an airplane flight through a convective cloud.

Observational data in mixing diagrams are commonly discussed in relation to the homogeneous mixing line, a curve of global steady states ( $r_s^3, n_s$ ) that result from homogeneous mixing (no complete evaporation) between different proportions of undiluted cloudy and dry environmental air (Gerber et al., 2008; Kumar et al., 2014; Pinsky et al., 2016a). Beals et al. (2015) calculated this line, it is also shown in Figure 5(a). A fundamental problem is however that it is not clear how to interpret mixing diagrams such as Figure 5(a), since it is not clear that the empirically observed droplet populations reflect global steady states (Pinsky and Khain, 2018a).

It is nevertheless likely that most data points in Figure 5(a) sample local steady states, i.e. locally well-mixed droplet populations that reside in saturated air. To describe such droplet populations, one must refer to the multi-

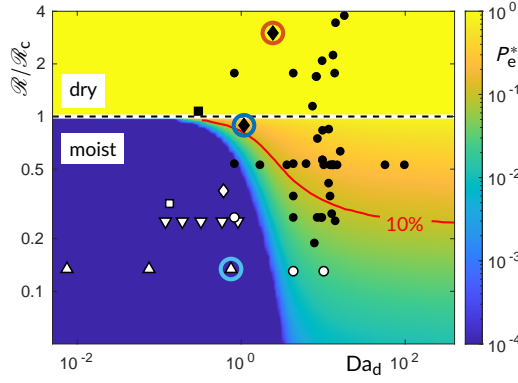


FIGURE 4 Steady-state fraction  $P_e^*$  of completely evaporated droplets, as a function of  $Da_d$  and  $R/R_c$ , details in SI. The fraction  $P_e^*$  is colour coded. The solid red line is the contour  $P_e^* = 10\%$ , the black dashed line indicates the transition between moist and dry steady states, and symbols indicate DNS results from previous studies:  $\triangle$  (Kumar et al., 2012),  $\square$  (Kumar et al., 2013),  $\diamond$  (Kumar et al., 2014),  $\nabla$  (Kumar et al., 2018), and  $\circ$  (Andrejczuk et al., 2006). Filled symbols indicate  $P_e^* > 10\%$ . The DNS of Andrejczuk et al. (2006) should not be quantitatively compared to the statistical model results, since they are for different initial conditions and decaying turbulence (see text and SI). Red, blue and light blue circles correspond to the dry, moist, and very moist simulations in Figures 2 and 3.

scale turbulent mixing process. We attempted this analysis using the statistical model, assuming that the statistical model with the initial condition shown Figure 1(b) describes how a cloud structure at the spatial scale  $L$  develops. Under this assumption,  $n_*$  and  $r_*^3$  are given by the droplet-number density (normalised by  $n_0$ ) and the mean cubed droplet radius  $\langle r(t)^3 \rangle$  in the steady state, and we can conjecture the mixing histories that formed the measured droplet populations.

We begin by noting that  $\chi$  and  $P_e^*$  are completely determined for any steady-state point  $(r_*^3, n_*)$  in a mixing diagram. To show this, we write the volume-averaged initial supersaturation as  $\langle s(0) \rangle = (1 + s_c)(\chi + \chi_0) - 1$ , where  $\chi_0$  is a constant that depends on the initial supersaturation profile (details in the SI). Inserting

$$\chi = n_* / (1 - P_e^*) \quad (4)$$

into  $\theta = -\langle s(t) \rangle - \frac{2\chi}{3\mathcal{R}} [1 - P_e(t)] \langle r^3(t) \rangle$  we find:

$$P_e^* = 1 - \frac{n_* [1 + \frac{3}{2}\mathcal{R}(1 + s_c)]}{n_* r_*^3 + \frac{3}{2}\mathcal{R} [1 - \chi_0(1 + s_c)]}. \quad (5)$$

Equations 4 and 5 determine how to map  $(r_*^3, n_*)$  to  $(\chi, P_e^*)$ . As a consistency check we note that one obtains the homogeneous mixing line (Pinsky et al., 2016a) from Equation 5 by setting  $P_e^* = 0$ . This allows us to infer that  $\mathcal{R} = 0.17$  and  $s_c = \chi_0 = 0$  from the homogeneous mixing line of Beals et al. (2015).

Any point in the mixing diagram must correspond to a local steady state with certain values of  $P_e^*$  and  $\chi$ . Each statistical-model simulation for given  $Da_d$ ,  $\mathcal{R}$ , and  $\chi$  yields a certain value of  $P_e^*$ . This allows us to extract a value of  $Da_d$  for each point in the mixing diagram from our statistical-model simulations. The result is shown in Figure 5(a). We see that  $Da_d$  increases rapidly above the homogeneous mixing line. Estimating  $\tau_s \sim 1$  s from Beals et al. (2015) and conservatively estimating  $\varepsilon \sim 1$  cm<sup>2</sup>s<sup>-3</sup> for a convective cloud, a value of  $Da_d = 1000$  implies that an observed droplet population was mixed at spatial scales of the order of  $L \sim \sqrt{\varepsilon \tau_L^3} \sim 5$  km, larger than the size of the cloud. In

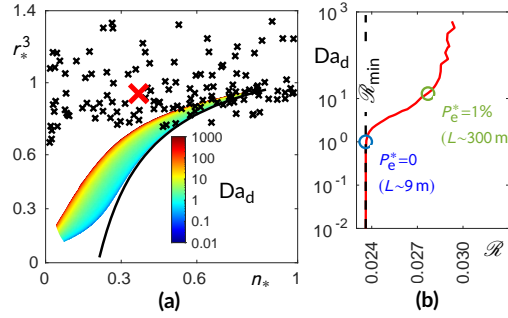


FIGURE 5 (a) Mixing diagram. Empirical data from Beals et al. (2015) (black crosses). The homogeneous mixing line (black) from top panel of Figure 3 of Beals et al. (2015) corresponds to  $\mathcal{R} = 0.17$ . The coloured region shows where steady states are found in the mixing diagram for  $\mathcal{R} = 0.17$ . The corresponding values of  $Da_d$  are colour coded (legend). The red cross is the measurement shown in the middle panel of Figure 2 of Beals et al. (2015). (b) Values of  $\mathcal{R}$  and  $Da_d$  consistent with a steady state at the red cross in panel (a) (red). We estimate  $L \sim 9$  m for  $Da_d = 1$  (blue circle). These local mixing processes have  $\mathcal{R} = \mathcal{R}_{\min}$  (black dashed line), so no droplets evaporated completely ( $P_e^* = 0$ ). The green circle corresponds to  $Da_d = 13$  and  $\mathcal{R} = 0.028$  with  $P_e^* = 1\%$  and  $L \sim 300$  m.

other words, the rapid increase of  $Da_d$  in Figure 5(a) suggests that most of the data in the mixing diagram cannot be in a global steady state of a mixing process parameterised by  $\mathcal{R} = 0.17$ .

We concluded above that most measurements of Beals et al. (2015) are likely to correspond to local steady states. As undiluted cloudy air is mixed with premixed air, such steady states are formed locally and temporarily as local mixing processes equilibrate at small spatial scales [Figure 1(a)]. We now discuss how the analysis of local steady states may yield insight into possible local histories of the cloud. Air affected by earlier mixing events is not as dry as environmental air, so the mixing of undiluted cloud with premixed air is governed by smaller values of  $\mathcal{R}$ . We therefore ask: which values of  $\mathcal{R}$  are consistent with the assumption that the experimentally observed droplet population in the middle panel of Figure 2 of Beals et al. (2015) – red cross in Figure 5(a) – reflects a local steady state? Our model allows us to determine possible combinations of  $Da_d$ ,  $\mathcal{R}$ , and  $\chi$  consistent with a local steady state. We know that  $\mathcal{R}$  must be smaller than 0.17, the upper limit dictated by the homogeneous mixing line of Beals et al. (2015). Furthermore, since the data cannot lie below the homogeneous mixing line of the global mixing process, a lower bound for  $\mathcal{R}$  is  $\mathcal{R}_{\min} = \frac{2}{3}(n_* - r_*^3)n_* / [(1 + s_c)(\chi_0 + n_*) - 1] = 0.0236$ .

Figure 5(b) shows values of  $\mathcal{R}$  and  $Da_d$  obtained from our statistical-model simulations that are consistent with these constraints. We see that the range of possible values of  $Da_d$  covers several orders of magnitude. This means that local mixing processes consistent with the red cross in Figure 5(a) may have occurred over a large range of spatial scales. We also see that  $\mathcal{R}$  does not vary much in Figure 5(b), only between 0.024 and 0.03. This allows us to conclude that some important aspects of the mixing dynamics are essentially independent of spatial scale. First, the fact that  $\mathcal{R}$  is substantially smaller than 0.17 indicates that the non-cloudy air was premixed. Second, using Equation 5, we find that the reduction in droplet-number density was primarily caused by dilution even at the largest scales, since  $P_e^*$  increases only up to  $\sim 1.4\%$  for the largest value of  $Da_d$ , at  $Da_d \sim 1000$  and  $\mathcal{R} = 0.03$ . Put differently,  $\chi \sim n_*$  for all values of  $Da_d$  we considered.

How does the outcome of a local mixing process depend on its scale? Larger scales correspond to larger values of  $Da_d$ , and Figure 5(b) shows that complete droplet evaporation begins to occur around  $Da_d = 1$ , where  $\mathcal{R}$  starts to exceed  $\mathcal{R}_{\min}$  (blue circle). Estimating  $\varepsilon \sim 10 \text{ cm}^2 \text{ s}^{-3}$ , a typical value for convective clouds (Devenish et al., 2012), we find that  $Da_d = 1$ ,  $\tau_s \sim 1$ , and  $\mathcal{R} = \mathcal{R}_{\min}$  correspond to the spatial scale 9 m. Mixing processes leading to the red cross

in Figure 5(a) that occurred at scales smaller than 9 m were therefore perfectly homogeneous: none of the droplets evaporated completely as they were diluted by premixed air. At larger spatial scales, small but non-zero fractions of the droplets evaporated completely. Equation 5 gives  $\mathcal{R} = 0.028$  for  $P_e^* = 1\%$ , and from Figure 5(b) we read off  $\text{Da}_d = 13$  (green circle). For  $\varepsilon \sim 10 \text{ cm}^2 \text{ s}^{-3}$  these values correspond to 300 m. This suggests that reductions in droplet number concentration are dominated by dilution, and not complete droplet evaporation, also for mixing processes that range over hundreds of meters. Furthermore, since most data points in Figure 5(a) reside well above the region where equilibria are found for  $\mathcal{R} = 0.17$ , we conclude that they too resulted from mixing with premixed air.

## 4 | DISCUSSION

A general conclusion from our analysis is that both Damköhler numbers are important for the transition to inhomogeneous mixing:  $\text{Da}_d$  parameterises the mixing-limited nature of droplet evaporation, and the ratio  $\mathcal{R} = \text{Da}_d / \text{Da}_s$  regulates the self-limiting effect of droplet evaporation, namely that droplets cease to evaporate when they have saturated the surrounding air or evaporated completely. Analysing the parameters of our microscopic equations 1 we see that  $\mathcal{R} = -\frac{3}{2}R$  where  $R$  is the potential evaporation parameter of Pinsky et al. (2016a) and Pinsky and Khain (2018a). So  $R$  is in fact given by the ratio of  $\text{Da}_d$  and  $\text{Da}_s$ , consistent with our conclusion that both Damköhler numbers matter.

Pinsky and Khain (2018b, 2019) concluded that the Damköhler number ratio  $\mathcal{R}$  determines whether a cloud expands by dilution or shrinks by complete droplet evaporation. A mixing process that mixes equal proportions of saturated cloudy and subsaturated non-cloudy air has  $\mathcal{R}_c = \frac{2}{3}$ , so the symmetric configuration they adopted for the cloud edge implies that the cloud expands if  $\mathcal{R} < \frac{2}{3}$ , and shrinks otherwise. We note that whether the cloud expands or shrinks depends on the position and scale at which one perceives it. A local mixing process with small  $\mathcal{R} / \mathcal{R}_c$  tends towards a moist steady state, so the cloud dilutes locally. A local mixing process that tends towards a dry steady state, by contrast, consumes the cloud. It is possible for a cloud to expand locally for some time, even if this local expansion is part of a mixing process that consumes the cloud at larger length and time scales. Although global mixing processes are transient, they contain local steady states. Diluted and saturated local droplet populations [such as the red cross in Figure 5(a)] can be a part of such transients. However, such local steady states must eventually be abandoned as mixing proceeds globally.

Adopting this multi-scale picture of mixing, in which a large-scale mixing process consists of many mixing processes at smaller scales, it is natural to expect that large ranges of the parameters  $\chi$ ,  $\mathcal{R}$  and  $\text{Da}_d$  are relevant. If one moves the domain of a local mixing process from the interior of the cloud towards the cloud edge, the liquid water content decreases, so that  $\mathcal{R} / \mathcal{R}_c$  and  $\text{Da}_d$  increase. Lehmann et al. (2009) point out that  $\text{Da}_d$  increases as one perceives mixing processes at larger and larger spatial scales. This corresponds to moving to the right in Figure 4. We note that  $\mathcal{R} / \mathcal{R}_c$  and  $\text{Da}_d$  tend to increase with distance from the interior of the cloud. Moving the sampling volume towards the cloud edge then corresponds to a motion upwards and to the right in Figure 4. The amount of complete droplet evaporation increases in this direction, consistent with the fact that complete droplet evaporation takes place at the cloud edge.

A number of assumptions may influence our interpretation of the empirical data in Section 3.2. First, the model configuration in Figure 1(b) is simplified compared to real clouds, which have irregular shapes that deform during the mixing-evaporation process. Second, the observational method may not detect droplets with radii smaller than  $3 \mu\text{m}$  ( $r_a^3 = 0.2$ ), as stated by Beals et al. (2015). If many small droplets were not detected, the observations in Figure 5(a) are located too far from the homogeneous mixing line. Third, at the upper end of the Damköhler range in Figure 5, the statistical model may not be quantitatively accurate, as stated above. We nevertheless expect that the statistical

model reproduces the evolution of droplet-size distributions in DNS qualitatively in Figure 5. This expectation is corroborated by the robust tendency for  $P_e^*$  to increase with increasing values of  $Da_d$  and  $\mathcal{R}$  in Figure 4, and follows directly from the roles of the Damköhler numbers in mixing-evaporation dynamics.

The deviations in the tails of droplet-size distributions at moderate Damköhler numbers in Figure 3 suggest that the next step in improving the statistical model should aim at reproducing the fastest evaporation rates in the transient mixing-evaporation process. A better agreement in the tails could be achieved by refining the closure for supersaturation diffusion by using a dynamic  $C_\phi$  in Equation 3b (Jenny et al., 2012), or by introducing additional fluctuations (Pope, 1991). Another possibility is to refine the description of the spatial structure of the supersaturation field by improved closures (Vedula et al., 2001; Pope, 1991; Meyer and Jenny, 2008; Jenny et al., 2012)

## 5 | CONCLUSIONS

We derived a statistical model for evaporation and turbulent mixing at the cloud edge from first principles. The model explains results of earlier DNS studies of mixing (Andrejczuk et al., 2006; Kumar et al., 2012, 2013, 2014, 2018), and shows that two thermodynamic time scales are important for a mixing process, the droplet evaporation time and the supersaturation relaxation time. This means that one must consider two Damköhler numbers in order to quantify the mixing-evaporation dynamics. We concluded that the simulations of Kumar et al. (2018) did not exhibit a transition to inhomogeneous mixing with increasing spatial scale because the supersaturation relaxation time was too small compared to the droplet evaporation time.

Our analysis supports general conclusions regarding in-situ observation of droplets in turbulent clouds. First, most of the local and instantaneous snapshots of droplet configurations observed by Beals et al. (2015) cannot be in the steady states of a global mixing process that mixed undiluted cloud with dry environmental air. However, a local droplet population may still be in a local steady state, established as the droplets saturated the air locally. Such local steady states belong to the transient of a global mixing process. In order to understand the nature of this transient, it was necessary to consider the whole range of possible steady states at different length scales, Figure 1 (a). In short, clouds are not equilibrated at large scales, yet local steady states occur at small scales.

Our analysis also indicates that most of the droplet populations observed by Beals et al. (2015) are likely to have resulted from mixing with premixed air, and we concluded that the corresponding local steady states arose by dilution rather than complete evaporation. Our model indicates that only very few droplets evaporated completely.

We found that the statistical-model dynamics is somewhat slower than the DNS of Kumar et al. (2012, 2014), and that the tails of our droplet-size distributions are somewhat lighter. We speculated that this may be due to that the supersaturation dynamics is oversimplified. Since our model belongs to the family of established PDF models (Pope, 2000), it is clear how to address this question in the future (Vedula et al., 2001; Pope, 1991; Jenny et al., 2012).

Last but not least our analysis highlights which additional observational data is needed for a more quantitative statistical-model analysis of in-situ cloud-droplet measurements. To determine the three key parameters, the volume fraction of cloudy air as well as the two Damköhler numbers, one needs joint measurements of local droplet populations, supersaturation levels in their vicinity, and the sizes of the local cloud structures. This will allow to characterise and understand the mechanisms underlying local mixing processes observed on different length and time scales, and at different distances from the cloud edge. A challenge for the future is to understand the global picture, how evaporation distributes in the cloud, and where complete droplet evaporation takes place. This is necessary to improve the parameterisation of mixing and evaporation at the cloud edge in sub-grid scale models, in order to better represent the radiative effects of clouds.

## 6 | SUPPORTING INFORMATION

The SI contains Tables S1-S3 and Appendix S1. Table S1 lists all parameters of our statistical model simulations. Tables S2 and S3 specify the DNS results from Kumar et al. (2012, 2013, 2014, 2018), and Andrejczuk et al. (2006) in Figure 4. Appendix S1 describes the relation between our microscopic Equations 1, and those used in the DNS of others (Vaillancourt et al., 2002; Paoli and Shariff, 2009; Lanotte et al., 2009; Perrin and Jonker, 2015; Kumar et al., 2014, 2018). We discuss the approximations made in deriving Equations 1, and quantify their accuracy. We also describe how to derive the statistical model, Equations 3, from Equations 1, using the framework of PDF methods (Pope, 2000). We detail our computer simulations of the statistical model, and address their numerical convergence. Finally, Appendix S1 contains details concerning our interpretation of the data of Beals et al. (2015), and of direct numerical simulations conducted by other authors.

## ACKNOWLEDGEMENTS

JF and BM thank B. Kumar and J. Schumacher for providing details of their simulations. We acknowledge support by Vetenskapsrådet (grant number 2017-368 3865), Formas (grant number 2014-585), and by the grant 'Bottlenecks for particle growth in turbulent aerosols' from the Knut and Alice Wallenberg Foundation, Dnr. KAW 2014.0048. Simulations were performed on resources at Chalmers Centre for Computational Science and Engineering (C3SE) provided by the Swedish National Infrastructure for Computing (SNIC).

## 7 | LIST OF SYMBOLS

$t$	time
$\mathbf{x} = (x, y, z)$	spatial position
$N_0$	number of droplets at initialisation
$P_e$	fraction of completely evaporated droplets
$\mathbf{u}$	fluid velocity
$p$	pressure
$L$	side length of cubic simulation domain
$w$	width of initially cloudy region in simulation domain
$s_c$	supersaturation within initial cloud slab
$s_e$	supersaturation outside initial cloud slab
TKE	turbulent kinetic energy
$U$	root-mean-square of fluid velocity
$\varepsilon$	turbulent dissipation rate per unit mass
$\nu$	kinematic viscosity
$\kappa$	diffusivity of supersaturation
$s$	supersaturation
$r$	droplet radius
$r_0$	initial volume radius of droplets
$n_0$	droplet-number density of initially cloudy region
$\overline{r_\alpha(t)s(\mathbf{x}_\alpha, t)}$	average of $r_\alpha(t)s(\mathbf{x}_\alpha, t)$ for droplets in the vicinity of $\mathbf{x}$ at time $t$
$\frac{D}{Dt}$	Lagrangian time derivative
$\tau_d$	droplet evaporation time
$\tau_s$	supersaturation relaxation time
$\tau_\ell$	time scale for mixing at the length scale $\ell$
$\tau_L$	large-eddy turnover time in simulation domain
$Re_L$	turbulence Reynolds number
$Sc$	Schmidt number
$V$	non-dimensional volume of simulation domain
$Da_d$	Damköhler number based on droplet evaporation time
$Da_s$	Damköhler number based on supersaturation relaxation time
$\mathcal{R}$	Damköhler-number ratio
$\mathcal{R}_c$	Critical Damköhler-number ratio
$\mathcal{R}_{\min}$	Lower bound for Damköhler-number ratio related to mixing diagrams
$\chi$	volume fraction of cloudy air
$\chi_0$	contribution to the initial volume average of supersaturation
$\theta$	conserved quantity that reflects the conservation of water and energy
$C_0, C_\phi$	empirical constants
$\langle \dots \rangle$	volume average or ensemble average in statistical model

## REFERENCES

- Abade, G. C., Grabowski, W. W. and Pawlowska, H. (2018) Broadening of cloud droplet spectra through eddy hopping: Turbulent entraining parcel simulations. *Journal of the Atmospheric Sciences*, **75**, 3365–3379.
- Andrejczuk, M., Grabowski, W. W., Malinowski, S. P. and Smolarkiewicz, P. K. (2006) Numerical simulation of cloud–clear air interfacial mixing: Effects on cloud microphysics. *Journal of the Atmospheric Sciences*, **63**, 3204–3225.
- Baker, M. B., Corbin, R. G. and Latham, J. (1980) The influence of entrainment on the evolution of cloud droplet spectra: I. A model of inhomogeneous mixing. *Quarterly Journal of the Royal Meteorological Society*, **106**, 581–598.
- Beals, M. J., Fugal, J. P., Shaw, R. A., Lu, J., Spuler, S. M. and Stith, J. L. (2015) Holographic measurements of inhomogeneous cloud mixing at the centimeter scale. *Science*, **350**, 87–90.
- Blyth, A. M. (1993) Entrainment in cumulus clouds. *Journal of applied meteorology*, **32**, 626–641.
- Bodenschatz, E., Malinowski, S. P., Shaw, R. A. and Stratmann, F. (2010) Can we understand clouds without turbulence? *Science*, **327**, 970–971.
- Burnet, F. and Brenguier, J.-L. (2007) Observational study of the entrainment-mixing process in warm convective clouds. *Journal of the Atmospheric Sciences*, **64**, 1995–2011.
- Caldwell, P. M., Zelinka, M. D., Taylor, K. E. and Marvel, K. (2016) Quantifying the sources of intermodel spread in equilibrium climate sensitivity. *Journal of Climate*, **29**, 513–524.
- Chandrakar, K. K., Cantrell, W., Chang, K., Ciochetto, D., Niedermeier, D., Ovchinnikov, M., Shaw, R. A. and Yang, F. (2016) Aerosol indirect effect from turbulence-induced broadening of cloud-droplet size distributions. *Proceedings of the National Academy of Sciences*, **113**, 14243–14248.
- Devenish, B. J., Bartello, P., Brenguier, J.-L., Collins, L. R., Grabowski, W. W., IJzermans, R. H. A., Malinowski, S. P., Reeks, M. W., Vassilicos, J. C., Wang, L.-P. and Warhaft, Z. (2012) Droplet growth in warm turbulent clouds. *Quarterly Journal of the Royal Meteorological Society*, **138**, 1401–1429.
- Dimotakis, P. E. (2005) Turbulent Mixing. *Annual Review of Fluid Mechanics*, **37**, 329–356.
- Dufresne, J.-L. and Bony, S. (2008) An assessment of the primary sources of spread of global warming estimates from coupled atmosphere–ocean models. *Journal of Climate*, **21**, 5135–5144.
- Eswaran, V. and Pope, S. (1988) Direct numerical simulations of the turbulent mixing of a passive scalar. *Physics of Fluids*, **31**, 506–520.
- Frisch, U. (1995) *Turbulence: The Legacy of A. N. Kolmogorov*. Cambridge University Press.
- Gerber, H. E., Frick, G. M., Jensen, J. B. and Hudson, J. G. (2008) Entrainment, mixing, and microphysics in trade-wind cumulus. *J. Meteor. Soc. Japan*, **86A**, 87–106.
- Grabowski, W. W. and Wang, L.-P. (2013) Growth of cloud droplets in a turbulent environment. *Annual Review of Fluid Mechanics*, **45**, 293–324.
- Gustavsson, K. and Mehlig, B. (2016) Statistical models for spatial patterns of heavy particles in turbulence. *Advances in Physics*, **65**, 1–57.
- Haworth, D. C. (2010) Progress in probability density function methods for turbulent reacting flows. *Progress in Energy and Combustion Science*, **36**, 168–259.
- Hoffmann, F. and Feingold, G. (2019) Entrainment and mixing in stratocumulus: Effects of a new explicit subgrid-scale scheme for large-eddy simulations with particle-based microphysics. *Journal of the Atmospheric Sciences*, **76**, 1955–1973.



- Jeffery, C. A. (2007) Inhomogeneous cloud evaporation, invariance, and Damköhler number. *J. Geophys. Res.*, **112**, D24S21.
- Jenny, P., Roekaerts, D. and Beishuizen, N. (2012) Modeling of turbulent dilute spray combustion. *Progress in Energy and Combustion Science*, **38**, 846–887.
- Kokhanovsky, A. (2004) Optical properties of terrestrial clouds. *Earth-Science Reviews*, **64**, 189–241.
- Kumar, B., Götzfried, P., Suresh, N., Schumacher, J. and Shaw, R. A. (2018) Scale dependence of cloud microphysical response to turbulent entrainment and mixing. *Journal of Advances in Modeling Earth Systems*, **10**, 2777–2785.
- Kumar, B., Janetzko, F., Schumacher, J. and Shaw, R. A. (2012) Extreme responses of a coupled scalar–particle system during turbulent mixing. *New J. Phys.*, **14**, 115020.
- Kumar, B., Schumacher, J. and Shaw, R. A. (2013) Cloud microphysical effects of turbulent mixing and entrainment. *Theor. Comp. Fluid Dyn.*, **27**, 361–376.
- (2014) Lagrangian mixing dynamics at the cloudy–clear air interface. *Journal of the Atmospheric Sciences*, **71**, 2564–2580.
- Lamb, D. and Verlinde, J. (2011) *Physics and Chemistry of Clouds*. Cambridge University Press.
- Lanotte, A. S., Seminara, A. and Toschi, F. (2009) Cloud droplet growth by condensation in homogeneous isotropic turbulence. *Journal of the Atmospheric Sciences*, **66**, 1685–1697.
- Lehmann, K., Siebert, H. and Shaw, R. A. (2009) Homogeneous and inhomogeneous mixing in cumulus clouds: Dependence on local turbulence structure. *Journal of the Atmospheric Sciences*, **66**, 3641–3659.
- Li, X.-Y., Brandenburg, A., Svensson, G., Haugen, N. E. L., Mehlig, B. and Rogachevskii, I. (2020) Condensational and collisional growth of cloud droplets in a turbulent environment. *Journal of the Atmospheric Sciences*, **77**, 337–353.
- Lu, C., Liu, Y., Zhu, B., Yum, S. S., Krueger, S. K., Qiu, Y., Niu, S. and Luo, S. (2018) On which microphysical time scales to use in studies of entrainment-mixing mechanisms in clouds. *J. Geophys. Res. Atmos.*, **123**, 3740–3756.
- Mauritsen, T., Stevens, B., Roeckner, E., Crueger, T., Esch, M., Giorgetta, M., Haak, H., Jungclaus, J., Klocke, D., Matei, D., Mikolajewicz, U., Notz, D., Pincus, R., Schmidt, H. and Tomassini, L. (2012) Tuning the climate of a global model. *Journal of Advances in Modeling Earth Systems*, **4**, 1–18.
- Meyer, D. W. and Jenny, P. (2008) An improved mixing model providing joint statistics of scalar and scalar dissipation. *Combustion and Flame*, **155**, 490–508.
- Paoli, R. and Shariff, K. (2009) Turbulent condensation of droplets: Direct simulation and a stochastic model. *Journal of the Atmospheric Sciences*, **66**, 723–740.
- Perrin, V. E. and Jonker, H. J. J. (2015) Lagrangian droplet dynamics in the subsiding shell of a cloud using direct numerical simulations. *Journal of the Atmospheric Sciences*, **72**, 4015–4028.
- Pincus, R., Winker, D., Bony, S. and Stevens, B. (2018) *Shallow Clouds, Water Vapor, Circulation, and Climate Sensitivity*. Springer.
- Pinsky, M. and Khain, A. (2018a) Theoretical analysis of mixing in liquid clouds – Part IV: DSD evolution and mixing diagrams. *Atmos. Chem. Phys.*, **18**, 3659–3676.
- (2018b) Theoretical analysis of the entrainment–mixing process at cloud boundaries. Part I: Droplet size distributions and humidity within the interface zone. *Journal of the Atmospheric Sciences*, **75**, 2049–2064.
- (2019) Theoretical analysis of the entrainment–mixing process at cloud boundaries. Part II: Motion of cloud interface. *Journal of the Atmospheric Sciences*, **76**, 2599–2616.
- Pinsky, M., Khain, A. and Korolev, A. (2016a) Theoretical analysis of mixing in liquid clouds – Part 3: Inhomogeneous mixing. *Atmos. Chem. Phys.*, **16**, 9273–9297.

- Pinsky, M., Khain, A., Korolev, A. and Magaritz-Ronen, L. (2016b) Theoretical investigation of mixing in warm clouds – Part 2: Homogeneous mixing. *Atmos. Chem. Phys.*, **16**, 9255–9272.
- Pope, S. (1991) Mapping closures for turbulent mixing and reaction. *Theoretical and Computational Fluid Dynamics*, **2**, 255–270.
- Pope, S. B. (1985) PDF methods for turbulent reactive flows. *Progress in Energy and Combustion Science*, **11**, 119–192.
- (2000) *Turbulent Flows*. Cambridge University Press.
- (2011) Simple models of turbulent flows. *Physics of Fluids*, **23**, 1–20.
- Pope, S. B. and Chen, Y. L. (1990) The velocity-dissipation probability density function model for turbulent flows. *Physics of Fluids*, **2**, 1437–1449.
- Rogers, R. R. and Yau, M. K. (1989) *A Short Course in Cloud Physics*. Pergamon Press.
- Sardina, G., Picano, F., Brandt, L. and Caballero, R. (2015) Continuous growth of droplet size variance due to condensation in turbulent clouds. *Physical Review Letters*, **115**, 184501.
- Sardina, G., Poulain, S., Brandt, L. and Caballero, R. (2018) Broadening of cloud droplet size spectra by stochastic condensation: Effects of mean updraft velocity and CCN activation. *Journal of the Atmospheric Sciences*, **75**, 451–467.
- Shraiman, B. I. and Siggia, E. D. (2000) Scalar turbulence. *Nature*, **405**, 639–646.
- Siewert, C., Bec, J. and Krstulovic, G. (2017) Statistical steady state in turbulent droplet condensation. *Journal of Fluid Mechanics*, **810**, 254–280.
- Stocker, T., Qin, D., Plattner, G.-K., Tignor, M., Allen, S., Boschung, J., Nauels, A., Xia, Y., Bex, V. and Midgley, P. (eds.) (2013) *Climate Change 2013: The Physical Science Basis. Contribution of Working Group I to the Fifth Assessment Report of the Intergovernmental Panel on Climate Change*. Cambridge University Press.
- Stöllinger, M., Naud, B., Roekaerts, D., Beishuizen, N. and Heinz, S. (2013) PDF modeling and simulations of pulverized coal combustion–Part 1: Theory and modeling. *Combustion and Flame*, **160**, 384–395.
- Szumowski, M. J., Rauber, R. M., Ochs III, H. T. and Beard, K. V. (1998) The microphysical structure and evolution of Hawaiian rainband clouds. Part II: Aircraft measurements within rainbands containing high reflectivity cores. *Journal of the Atmospheric Sciences*, **55**, 208–226.
- Szumowski, M. J., Rauber, R. M., Ochs III, H. T. and Miller, L. (1997) The microphysical structure and evolution of Hawaiian rainband clouds. Part I: Radar observations of rainbands containing high reflectivity cores. *Journal of the Atmospheric Sciences*, **54**, 369–385.
- Tölle, M. H. and Krueger, S. K. (2014) Effects of entrainment and mixing on droplet size distributions in warm cumulus clouds. *Journal of Advances in Modeling Earth Systems*, **6**, 281–299.
- Vaillancourt, P. A., Yau, M. K., Bartello, P. and Grabowski, W. W. (2002) Microscopic approach to cloud droplet growth by condensation. Part II: Turbulence, clustering, and condensational growth. *Journal of the Atmospheric Sciences*, **59**, 3421–3435.
- Vaillancourt, P. A., Yau, M. K. and Grabowski, W. W. (2001) Microscopic approach to cloud droplet growth by condensation. Part I: Model description and results without turbulence. *Journal of the Atmospheric Sciences*, **58**, 1945–1964.
- Vedula, P., Yeung, P. and Fox, R. O. (2001) Dynamics of scalar dissipation in isotropic turbulence: a numerical and modelling study. *Journal of Fluid Mechanics*, **433**, 29.

---

**SUPPORTING INFORMATION**

---

# Supporting Information for "Key parameters for droplet evaporation and mixing at the cloud edge"

J. Fries<sup>1</sup> | G. Sardina<sup>2</sup> | G. Svensson<sup>3</sup> | B. Mehlig<sup>1</sup>

<sup>1</sup>Department of Physics, Gothenburg University, SE-41296 Gothenburg, Sweden

<sup>2</sup>Department of Mechanics and Maritime Sciences, Division of Fluid Dynamics, Chalmers University of Technology, SE-41296 Gothenburg, Sweden

<sup>3</sup>Department of Meteorology, Stockholm University and Swedish e-science Research Centre, Stockholm, Sweden

## Correspondence

Bernhard Mehlig, Department of Physics, Gothenburg University, SE-41296 Gothenburg, Sweden  
Email: bernhard.mehlig@physics.gu.se

This Supporting Information (SI) contains:

**Appendix S1**

**Tables S1 to S3**

**SI References**

# Appendix S1

## S1.1 | MICROSCOPIC EQUATIONS

We denote fluid velocity and pressure by  $\mathbf{u}(\mathbf{x}, t)$  and  $p(\mathbf{x}, t)$ . Additional fields are the supersaturation  $s(\mathbf{x}, t)$ , and the condensation rate  $C_d(\mathbf{x}, t)$ . Initially, at  $t = 0$ , there are  $N_0$  spherical droplets, labeled by  $\alpha = 1, \dots, N_0$ , with positions  $\mathbf{x}_\alpha(t)$ , velocities  $\mathbf{v}_\alpha(t)$ , and radii  $r_\alpha(t)$ . Our microscopic equations read:

$$\frac{\partial \mathbf{u}}{\partial t} + (\mathbf{u} \cdot \nabla) \mathbf{u} = -\frac{1}{\varrho_a} \nabla p + \nu \nabla^2 \mathbf{u}, \quad \nabla \cdot \mathbf{u} = 0, \quad (\text{S1.1a})$$

$$\frac{\partial s}{\partial t} + (\mathbf{u} \cdot \nabla) s = \kappa \nabla^2 s - A_2 C_d(\mathbf{x}, t) \quad (\text{S1.1b})$$

$$\text{with } C_d(\mathbf{x}, t) = \sum_{\alpha=1}^{N_0} G(|\mathbf{x} - \mathbf{x}_\alpha(t)|) \frac{4\pi}{3} \varrho_w \frac{dr_\alpha(t)^3}{dt} \quad (\text{S1.1c})$$

$$\frac{d\mathbf{x}_\alpha}{dt} = \mathbf{u}(\mathbf{x}_\alpha(t), t), \quad (\text{S1.1d})$$

$$\frac{dr_\alpha^2}{dt} = 2A_3 s(\mathbf{x}_\alpha(t), t). \quad (\text{S1.1e})$$

Here,  $\varrho_a$  is the density of air and  $\nu$  is its kinematic viscosity,  $\varrho_w$  is the density of pure liquid water,  $\kappa$  is the diffusivity of supersaturation, and  $A_2$  and  $A_3$  are thermodynamic coefficients. In Equation S1.1c,  $G(|\mathbf{x} - \mathbf{x}_\alpha(t)|)$  is a spatial kernel, normalised to unity. It makes it possible to construct the continuous condensation-rate field from the dispersed droplets, and ensures that the condensation rate is computed locally (Jenny et al., 2012). The supersaturation is defined as

$$s = e_v / e_{vs}(T) - 1, \quad (\text{S1.2})$$

where  $e_v$  is the partial pressure of water vapour and  $e_{vs}(T)$  is the equilibrium water-vapour pressure at the temperature  $T$  (Rogers and Yau, 1989). The partial pressure of water vapour depends on the density  $\varrho_v$  and gas constant  $R_v$  of water vapor, and is given by the ideal-gas law (Rogers and Yau, 1989):

$$e_v = \varrho_v R_v T. \quad (\text{S1.3})$$

Equations S1.1 describe an incompressible flow with advected droplets that condense or evaporate in response to the supersaturation in their vicinity. Evaporation or condensation causes the droplet radii  $r_\alpha$  to decrease or increase, at a rate regulated by the thermodynamic coefficient  $A_3$ . The supersaturation  $s(\mathbf{x}, t)$  evolves according to an advection-diffusion equation, with a source term that describes the response of  $s(\mathbf{x}, t)$  to droplet phase change. The strength of this response is regulated by the thermodynamic coefficient  $A_2$ . The parameters  $\varrho_a$ ,  $\nu$ ,  $\kappa$ ,  $\varrho_w$ ,  $A_2$ , and  $A_3$  are assumed constant in time. In addition, we impose that a droplet that has evaporated completely must remain at  $r_\alpha = 0$ .

Equation S1.1e relies on a scale separation: spatial scales of supersaturation fluctuations induced by turbulent mixing are much larger than the radii of droplets (Vaillancourt et al., 2001). This means that droplets do not impose boundary conditions on the supersaturation  $s(\mathbf{x}, t)$  in Equation S1.1b. They do interact locally with the supersaturation field, but over a finite volume determined by the spatial kernel in Equation S1.1c. It also means that the supersaturation  $s(\mathbf{x}, t)$  is not defined on length scales comparable to the radii of droplets, and therefore no a microscopic field in the most strict sense.

The microscopic equations S1.1 can be derived from more fundamental descriptions (Vaillancourt et al., 2001, 2002; Kumar et al., 2014, 2018; Perrin and Jonker, 2015). In the following we discuss the assumptions underlying Equations S1.1.

### S1.1.1 | Droplet inertia and settling

Equation S1.1d assumes that the droplets are small enough so that droplet inertia and settling are negligible (Gustavsson et al., 2014; Gustavsson and Mehlig, 2016). To neglect droplet inertia is a reasonable approximation when the Stokes number  $St = \tau_p / \tau_\eta$  is small enough. Here  $\tau_p = 2\rho_w r_\alpha^2 / (9\rho_a \nu)$  is the Stokes time for a small water droplet in air with  $\rho_w \gg \rho_a$ , and  $\tau_\eta = (\nu/\varepsilon)^{1/2}$  is the Kolmogorov time (of the order of the turnover time of the smallest eddies). Settling is negligible at small settling numbers  $Sv = g\tau_p / u_\eta$ , where  $u_\eta = (\nu\varepsilon)^{1/4}$  is the Kolmogorov velocity and  $g > 0$  is the gravitational acceleration. For typical cloud conditions (dissipation rate per unit mass  $\varepsilon \sim 10^{-2} \text{ m}^2/\text{s}^3$  and viscosity  $\nu \sim 1.5 \times 10^{-5} \text{ m}^2/\text{s}$ ), the Stokes number is of the order  $St \sim 10^{-4} (r_\alpha/\mu\text{m})^2$ , and  $Sv \sim 10^{-2} (r_\alpha/\mu\text{m})^2$ . In Figure 5 we analyse observational data from Beals et al. (2015). Droplet-size distributions in Beals et al. (2015) suggest that very few of the measured droplets exceed  $r_\alpha = 6 \mu\text{m}$ , corresponding to  $St = 1.4 \times 10^{-2}$  and  $Sv = 2.7 \times 10^{-1}$ . Droplet inertia and settling can therefore be neglected for most of these droplets. Out of the five DNS studies referred to in the main text, Kumar et al. (2013, 2014, 2018) incorporate droplet inertia and settling. Droplet inertia and settling can have minute effects on the droplet-size distribution, despite quite large settling numbers,  $Sv \sim 3.9$  (Kumar et al., 2013).

### S1.1.2 | Buoyancy

Buoyancy is neglected in the momentum equation, Equation S1.1a. The neglected buoyancy terms read (Bannon, 1996):

$$gB(\mathbf{x}, t) = g \left[ \frac{T - T_s(z)}{T_s(z)} + 0.608q_v - q_\ell \right]. \quad (\text{S1.4})$$

Here,  $B = B(\mathbf{x}, t)$  is buoyancy,  $T = T(\mathbf{x}, t)$  is temperature, and  $T_s(z)$  is a static base profile of temperature as a function of altitude  $z$ . Furthermore,  $q_v = q_v(\mathbf{x}, t)$  is the water-vapour mixing ratio, and  $q_\ell = q_\ell(\mathbf{x}, t)$  is the liquid-water mixing ratio. In a dry atmosphere ( $q_v = q_\ell = 0$ ), buoyancy variations are caused only by vertical displacements. If  $T_s(z)$  depends linearly on  $z$ , then a parcel that is neutrally buoyant at  $z = 0$  and is displaced adiabatically to an altitude  $z$  has the buoyancy

$$B = \frac{1}{T_s(0)} \left( \Gamma - \frac{dT_s}{dz} \right) z + O(z^2). \quad (\text{S1.5})$$

Here,  $\Gamma$  is the dry adiabatic lapse rate, the vertical temperature gradient  $dT/dz$  in a dry adiabatic atmosphere at hydrostatic equilibrium (Rogers and Yau, 1989). One finds an upper bound for the buoyancy variations within a system of spatial scale  $\ell$  by substituting  $z = \ell$  in Equation S1.5. An analogous constraint is derived in Dougherty (Dougherty, 1961). Comparing buoyancy acceleration  $gB$  at a spatial scale  $\ell$  to the inertial acceleration  $(\varepsilon^2/\ell)^{1/3}$  at that scale, one obtains the Dougherty-Ozmidov length scale (Grachev et al., 2015):

$$\ell_B = \varepsilon^{1/2} \left( g \frac{1}{T_s(0)} \left| \Gamma - \frac{dT_s}{dz} \right| \right)^{-3/4}. \quad (\text{S1.6})$$

For typical atmospheric conditions [ $\varepsilon \sim 10^{-2} \text{ m}^2/\text{s}^3$ ,  $\Gamma \sim -10^{-2} \text{ K/m}$ ,  $dT_s/dz \sim -2 \times 10^{-3} \text{ K/m}$  (Dougherty, 1961)], one finds  $\ell_B \sim 45 \text{ m}$ . Under these conditions, buoyancy effects may matter on spatial scales larger than 45 m.

In a moist atmosphere, buoyancy varies not only as a consequence of vertical displacements, but also because droplets condense and evaporate. The largest impact of droplet phase change occurs in regions where mixing between cloudy and subsaturated air takes place (Vaillancourt and Yau, 2000). In such regions, buoyancy reduces as evaporating droplets absorb latent heat from the air. Grabowski (1993) show that sedimentation of droplets from 7 cm wide stationary filaments of cloudy air can amplify buoyancy reductions due to droplet evaporation by a factor  $\sim 10$  within 5 s. We argue however that such amplifications can not be expected in turbulent clouds, because buoyancy fluctuations at spatial scales  $\ell \sim 7 \text{ cm}$  are smoothened by turbulent dissipation at time scales  $\tau_\ell \sim (\ell^2/\varepsilon)^{1/3}$  that are smaller than 5 s, already at quite low dissipation rates. We therefore analyse buoyancy reductions caused by evaporation using the mixing curve of buoyancy (Siems et al., 1990), which does not take into account droplet sedimentation. This mixing curve gives an upper bound on the buoyancy reduction  $\Delta B$  that phase change induces when a volume fraction  $\chi$  of cloudy air is mixed with a volume fraction  $1 - \chi$  of non-cloudy air. This upper bound is achieved when the mixture equilibrates at a moist or dry steady state, and it is a definite function of the volume fraction  $\chi$ , the temperatures  $T_c$  and  $T_e$ , the water-vapour mixing ratios  $q_{vc}$  and  $q_{ve}$ , and the liquid-water mixing ratio  $q_{\ell c}$  (Grabowski, 1993). The subscripts c and e indicate values for the cloudy and non-cloudy mixing substrates. We estimate  $T_c \sim 257.9 \text{ K}$ ,  $q_{vc} \sim 3.1 \cdot 10^{-3}$ ,  $q_{\ell c} \sim 5.6 \cdot 10^{-4}$ ,  $T_e \sim 257.6$ , and  $q_{ve} \sim 2.7 \cdot 10^{-3}$  for the cloud and cloud environment observed by Beals et al. (2015) (see Section S1.8). From these estimates we compute the upper bound  $\Delta B \sim 10^{-3}$  for buoyancy reductions caused by droplet evaporation, using the mixing curve of buoyancy in Grabowski (1993). Comparing  $g\Delta B$  with the a typical inertial acceleration  $(\varepsilon^2/\ell)^{1/3}$  at the spatial scale  $\ell$ , we find that buoyancy accelerations due to evaporation are smaller than inertial accelerations for  $\ell < 100 \text{ m}$ .

One caveat is that buoyancy may cause large-scale anisotropies in the fluid motion. This can introduce additional complexity to droplet evaporation and mixing (Perrin and Jonker, 2015). Nevertheless, buoyancy is not a necessary ingredient in a model for these processes. Buoyancy is neglected in two of the DNS studies that we compare to (Kumar et al., 2012, 2013), as well as in the studies of Pinsky and Khain (2018) and Jeffery (2007).

### S1.1.3 | Temperature changes due to vertical air motion

Neglecting temperature changes due to vertical air motion is justified for systems that remain at a constant altitude and that are not too large or too moist, as we now explain. Given the spatial scale  $\ell$  of a system that remains at a fixed altitude, the maximal temperature changes caused by vertical air motion are comparable to  $\ell\Gamma$ . For the temperature to change by 1 K due to vertical air motion,  $\Gamma \sim 10^{-2} \text{ K/m}$  dictates that we must have  $\ell \sim 100 \text{ m}$ .

Temperature regulates droplet evaporation through supersaturation. Supersaturation is determined by the temperature  $T$  and the water-vapour density  $\rho_v$  according to Equations S1.2 and S1.3. For the values of  $\rho_v$  that imply saturation ( $s = 0$ ) at temperatures above 273.15 K, we find that a temperature change of 1 K causes the supersaturation to change by 0.07 or less in magnitude. In a quite moist system, where the supersaturation is smaller than this in magnitude everywhere, temperature changes due to vertical air motion can be more important than mixing for droplet evaporation. Since temperature changes due to vertical air motion increase with the spatial scale of the system, results obtained using Equations S1.1 may be inaccurate for systems at constant altitudes that are large and moist. Temperature changes due to vertical air motion are often neglected in studies of droplet evaporation (Kumar et al., 2012, 2013, 2012, 2014, 2018; Andrejczuk et al., 2006; Pinsky and Khain, 2018; Siewert et al., 2017; Jeffery, 2007).

### S1.1.4 | Temperature and pressure dependence of the coefficient $A_3$

We use a constant thermodynamic coefficient  $A_3$ . This parameter is given by

$$A_3 = \left[ \left( \frac{\Lambda}{R_v T} - 1 \right) \frac{\Lambda \rho_w}{K_a T} + \frac{\rho_w R_v T}{D_v e_s(T)} \right]^{-1}, \quad (\text{S1.7})$$

where  $\Lambda$  is the latent heat of water vapor,  $K_a$  is the thermal conductivity of air, and  $D_v$  is the diffusivity of water vapour (Rogers and Yau, 1989). The parameter  $A_3$  decreases with pressure through  $D_v$ , and increases with the temperature  $T$  (Rogers and Yau, 1989). The values that we use for  $A_3$  are computed from temperatures and pressures that are representative of the systems that we consider. To use a constant value for  $A_3$  is usually a good approximation (Lanotte et al., 2009; Sardina et al., 2015; Lehmann et al., 2009; Kumar et al., 2012; Andrejczuk et al., 2009; Siewert et al., 2017; Jeffery, 2007; Pinsky and Khain, 2018; Devenish et al., 2016). The reason is that the temperature and pressure dependencies are quite weak. From Figure 7.1 of Rogers and Yau (1989) we see, for example, that  $A_3$  increases by 26% as the temperature increases from 10°C to 20°C and the pressure decreases from 100 kPa to 70 kPa. For observations of a convective cloud at 4000 m altitude (Beals et al., 2015) we estimate the temperature variations to be smaller than  $\sim 1^\circ\text{C}$  (see Section S1.8). These temperature variations cause  $A_3$  to change by less than 10%, which suggests that it is a good approximation to keep the coefficient constant in analyses of convective clouds at fixed altitude.

### S1.1.5 | Linearisation of the supersaturation profile

We treat the joint effect of temperature and water vapour at the level of a single field, the supersaturation field. This one-field treatment is obtained by linearising the supersaturations dependence on water-vapour mixing ratio  $q_v$  and temperature  $T$ , and by setting the diffusivities of water vapour and temperature equal to the same value  $\kappa$ . With the same diffusivity for temperature and water vapor, and with  $s$  given by a linear combination of  $q_v$  and  $T$ , the two separate advection-diffusion equations for temperature and water-vapour mixing ratio (Vaillancourt et al., 2001) can be concatenated into a single equation for  $s$ .

We denote the heat capacity of dry air at constant pressure by  $c_p$  and estimate  $\rho_a c_p \sim 1000 \text{ J}/(\text{m}^3\text{K})$  (Rogers and Yau, 1989). With this estimate, Table 7.1 of (Rogers and Yau, 1989) implies that the diffusivity of water vapour roughly equals the diffusivity of temperature for atmospheric conditions, so that it is sufficient to consider just one value for the diffusivity. The supersaturation lineqrised around a reference state with temperature  $T_r$  and water-vapour mixing ratio  $q_{vr}$  reads:

$$s(q_v, T) = s(q_{vr}, T_r) + \left. \frac{\partial s}{\partial q_v} \right|_{q_{vr}} (q_v - q_{vr}) + \left. \frac{\partial s}{\partial T} \right|_{q_{vr}} (T - T_r). \quad (\text{S1.8})$$

Using  $dq_v = -dq_\ell$  and  $dT = (\Lambda/c_p)dq_\ell$ , we find that the coefficient  $A_2$  in Equation S1.1b is given by

$$A_2 = \frac{1}{\rho_a} \left( \left. \frac{\partial s}{\partial q_v} \right|_{q_{vr}} - \frac{\Lambda}{c_p} \left. \frac{\partial s}{\partial T} \right|_{q_{vr}} \right). \quad (\text{S1.9})$$

In Figures 2 to 4 we compare our statistical-model results with DNS results (Kumar et al., 2014, 2018; Andrejczuk et al., 2009) that are obtained using models where temperature and water vapour are treated as two separate fields. In order to match their non-linear supersaturation to our linear supersaturation given by Equation S1.8, we linearise their supersaturation around a saturated reference state  $(T_r, q_{vr})$ . We use  $T_r = 270.77 \text{ K}$  (Kumar et al., 2014),  $T_r = 282.866 \text{ K}$  (Kumar et al., 2018), and  $T_r = 293 \text{ K}$  (Andrejczuk et al., 2009), determining our values of  $q_{vr}$  through Equations S1.2,

S1.3, and  $q_v = \rho_v / \rho_a$ . For a convective cloud observed by Beals et al. (2015) we estimate the temperatures  $T_c \sim 257.9$  and  $T_e \sim 257.6$ , and the water-vapour mixing ratios  $q_{vc} \sim 3.1 \times 10^{-3}$  and  $q_{ve} \sim 2.7 \times 10^{-3}$ , within and outside the cloud (see Section S1.8). Over these ranges, the absolute error of the supersaturation linearised at  $(T_r, q_{vr}) = (T_c, q_{vc})$  is less than 1%. The relative error at  $(T_e, q_{ve})$  is around 2%.

## S1.2 | INITIAL CONDITIONS

To allow for quantitative comparisons with the results of Kumar et al. (2013, 2012, 2014, 2018), we use the same (or almost identical) initial conditions: a slab of cloudy air inside a cubic domain of size  $L$  with periodic boundary conditions. The cloudy air occupies a fraction  $\chi$  of the domain, and it is surrounded by subsaturated air [Figure 1(b)]. The initial droplet-size distribution is either monodisperse or Gaussian, with mean  $r_\mu$  and standard deviation  $\sigma_0$ . When we compare to DNS from Kumar et al. (2013, 2012, 2014, 2018) in Figures 2 to 4, we use their initial droplet-size distribution, which is monodisperse ( $\sigma_0 = 0$ ). When we analyse measurements of Beals et al. (2015), we use the Gaussian droplet-size distribution of the undiluted cloud that corresponds to the measurements ( $\sigma_0 \neq 0$ , see Section S1.5). The simulations of Andrejczuk et al. (2006) are for decaying turbulence with quite strong buoyancy effects, and a different initial geometry. Nevertheless, some of our results can be compared qualitatively to the results of Andrejczuk et al. (2006), as explained in Section S1.7. Our analysis of the measurements of Beals et al. (2015) is based on our initial condition. This analysis rests upon the assumption that our system models a structure of size  $L$  formed at the cloud edge, although its detailed composition and geometry can deviate from our slab-like initial conditions.

Our initial conditions are homogeneous in two of the three coordinate axes. We take  $x$  to denote the coordinate in the spatially inhomogeneous direction. Initially the droplets are distributed uniformly and randomly within a three-dimensional cloud slab, the volume for which  $-\chi L/2 < x < \chi L/2$  [Figure 1(b)]. The initial droplet-number density of the slab is  $n_0 = N_0/(\chi V)$ , where  $V = L^3$  is the domain volume. To obtain the statistical-model results shown in Figures 2 to 4 we use the initial supersaturation profiles of Kumar et al. (2013, 2012, 2014, 2018):

$$s(x, 0) = (s_c - s_e) \exp \left[ -\zeta_1 \left( \frac{x}{L} \right)^{\zeta_2} \right] + s_e. \quad (\text{S1.10})$$

Here,  $s_c > 0$  and  $s_e < 0$  denote the initial supersaturation at the center of the slab and of the dry air [Figure 1(b)]. The shape of the initial supersaturation profile is contained in the parameters  $\zeta_1$  and  $\zeta_2$ . The homogeneous mixing line of Beals et al. (2015) passes through the top-right corner of the mixing diagram in Figure 5(a). To be able to compare with this homogeneous mixing line, we use a sharp initial supersaturation profile with  $s_c = 0$  when analysing the measured data:

$$s(x, 0) = \begin{cases} 0 & \text{for } |x/L| < \chi/2, \\ s_e & \text{otherwise.} \end{cases} \quad (\text{S1.11})$$

## S1.3 | NON-DIMENSIONAL EQUATIONS AND PARAMETERS

We non-dimensionalise Equations S1.1 using  $U = \sqrt{2\text{TKE}/3}$  and the large-eddy time  $\tau_L = \text{TKE}/\varepsilon$ , which is proportional to  $L/U$  if the size of the largest eddies scale with  $L$  (Pope, 2000). In addition, we use the following quantities to non-dimensionalise: the droplet-number density of the slab [ $n_0 = N_0/(\chi V)$ ], the (positive) supersaturation  $|s_e|$ , and the



initial volume radius

$$r_0 = \left[ \frac{1}{N_0} \sum_{\alpha=1}^{N_0} r_{\alpha}(0)^3 \right]^{\frac{1}{3}}. \quad (\text{S1.12})$$

We non-dimensionalise as follows:  $\mathbf{u}' = \mathbf{u}/U$ ,  $\mathbf{x}' = \mathbf{x}/(U\tau_L)$ ,  $t' = t/\tau_L$ ,  $p' = p/(\varrho_a U^2)$ ,  $\mathbf{x}'_{\alpha} = \mathbf{x}_{\alpha}/(U\tau_L)$ ,  $s' = s/|s_e|$ ,  $r'_{\alpha} = r_{\alpha}/r_0$ ,  $G' = G(U\tau_L)^3$ ,  $n' = n/n_0$ ,  $s'_c = s_c/|s_e|$ ,  $\sigma'_0 = \sigma_0/r_0$ ,  $L' = L/(U\tau_L)$  and  $V' = V/(U\tau_L)^3$ . Dropping the primes, Equations S1.1 take the non-dimensional form:

$$\frac{\partial \mathbf{u}}{\partial t} + (\mathbf{u} \cdot \nabla) \mathbf{u} = -\nabla p + \frac{1}{\text{Re}_L} \nabla^2 \mathbf{u}, \quad (\text{S1.13a})$$

$$\nabla \cdot \mathbf{u} = 0, \quad (\text{S1.13b})$$

$$\frac{\partial s}{\partial t} + (\mathbf{u} \cdot \nabla) s = \frac{1}{\text{Re}_L \text{Sc}} \nabla^2 s - \text{Da}_s \chi \overline{V r_{\alpha}(t) s(\mathbf{x}_{\alpha}, t)}, \quad (\text{S1.13c})$$

$$\frac{d\mathbf{x}_{\alpha}}{dt} = \mathbf{u}(\mathbf{x}_{\alpha}(t), t), \quad (\text{S1.13d})$$

$$\frac{dr_{\alpha}^2}{dt} = \text{Da}_d s(\mathbf{x}_{\alpha}(t), t). \quad (\text{S1.13e})$$

Here  $\overline{r_{\alpha}(t) s(\mathbf{x}_{\alpha}, t)}$  denotes the average of  $G(|\mathbf{x} - \mathbf{x}_{\alpha}(t)|) r_{\alpha}(t) s(\mathbf{x}_{\alpha}, t)$  over the droplets:

$$\overline{r_{\alpha}(t) s(\mathbf{x}_{\alpha}, t)} = \frac{1}{N_0} \sum_{\alpha=1}^{N_0} G(|\mathbf{x} - \mathbf{x}_{\alpha}(t)|) r_{\alpha}(t) s(\mathbf{x}_{\alpha}, t). \quad (\text{S1.14})$$

The average  $\overline{r_{\alpha}(t) s(\mathbf{x}_{\alpha}, t)}$  is position dependent, it depends on number and sizes of the local droplets, and upon the local supersaturation  $s(\mathbf{x}_{\alpha}, t)$  tied to these droplets. The dynamics in Equations S1.13 is identical to the dynamics in Equations S1.1, but non-dimensional.

Equations S1.13 have the following non-dimensional parameters: the domain volume  $V$ , the initial cloud fraction  $\chi$ , the turbulence Reynolds number  $\text{Re}_L = \frac{2}{3} \text{TKE}^2 / (\varepsilon \nu)$  (Pope, 2000), the Schmidt number  $\text{Sc} = \nu/\kappa$  [of order unity since the diffusivities of both temperature and water vapour are roughly the same as the kinematic viscosity of air (Perrin and Jonker, 2015)], and the two Damköhler numbers

$$\text{Da}_s = \tau_L/\tau_s \quad \text{and} \quad \text{Da}_d = \tau_L/\tau_d, \quad (\text{S1.15})$$

where  $\tau_s$  and  $\tau_d$  denote the supersaturation relaxation time and the droplet evaporation time. These time scales are given by

$$\tau_s = (4\pi A_2 A_3 \rho_w n_0 r_0)^{-1} \quad \text{and} \quad \tau_d = \frac{r_0^2}{2A_3 |s_e|}. \quad (\text{S1.16})$$

The time scales  $\tau_s$  and  $\tau_d$  can be very different. This can be understood by analysing their ratio

$$\mathcal{R} = \frac{\tau_s}{\tau_d} = \frac{\text{Da}_d}{\text{Da}_s} = \frac{|s_e|}{2\pi A_2 \rho_w n_0 r_0^3} = \frac{2|s_e|}{3A_2 \varrho_{\ell 0}}. \quad (\text{S1.17})$$

Here, we introduce  $\varrho_{\ell 0} = 4\pi r_0^3 n_0 \varrho_w / 3$  as a scale for liquid water density (mass per volume), the liquid water density in

a cloud with droplet-number density  $n_0$  and mean volume radius  $r_0$ . The scale for liquid water density determines  $\mathcal{R}$  together with the supersaturation  $s_e$  of the dry mixing substrate, and the thermodynamic coefficient  $A_2$ . For typical cloud conditions, we find  $A_2 \sim 260 \text{ m}^3/\text{kg}$  using Equation S1.9.

Consider, for example, a cumulus cloud with a typical (Rogers and Yau, 1989) liquid water density  $0.3 \text{ g/m}^3$  in the bulk that contains premixed and slightly subsaturated air with supersaturation  $-0.01$ . Substituting  $s_e = -0.01$  and  $\varrho_{\ell 0} = 0.3 \text{ g/m}^3$  into Equation S1.17, we find that  $\mathcal{R} \sim 0.09$  for the local mixing processes in the bulk, so  $\tau_d$  is more than ten times larger than  $\tau_s$ . At the cloud edge, by contrast, the liquid water density is lower, and mixing with dry air occurs. Assuming, say,  $s_e = -0.1$  and  $\varrho_{\ell 0} = 0.1 \text{ g/m}^3$  for a local mixing process yields  $\mathcal{R} = 2.6$ , so  $\tau_d$  is smaller than  $\tau_s$ . As we continue to move away from the cloud core,  $\varrho_{\ell 0}$  tends to zero, and  $\tau_s/\tau_d$  tends to infinity. In conclusion, the supersaturation relaxation time and the droplet evaporation time for local mixing processes can differ by orders of magnitude.

## S1.4 | STATISTICAL MODEL

The statistical model, Equations 3, rests upon on a probabilistic description of the microscopic Equations 1, in terms of two probability-density functions (PDF:s). The first PDF, denoted by  $\mathcal{F}$ , describes the droplets, and the second one, denoted by  $f$ , describes the air. The dynamics of Lagrangian fluid elements in Equations 3 constitutes a closed set of evolution equations for these PDF:s. The presence of droplets makes it necessary to consider two types of fluid elements, one for each PDF. Similar extensions of single-phase PDF models have already been made to describe combustion problems, where a gas interacts with droplets or other dispersed particles (Jenny et al., 2012; Stöllinger et al., 2013).

In the following, we derive the statistical model in terms of  $\mathcal{F}$  and  $f$ , since this allows us to highlight similarities and differences to PDF models for single-phase flows (Pope, 1985). The first step is to define the two PDF:s. Their exact evolution equations are not closed, as they contain conditional averages that are not known in terms of the PDF:s. We employ standard closures, designed to approximate the effects of acceleration and diffusive scalar flux in single-phase flows (Pope, 1985) and multiphase combustion (Jenny et al., 2012; Stöllinger et al., 2013; Haworth, 2010). The resulting closed set of equations constitutes a statistical model that describes the dynamics dictated by the microscopic Equations 1. As a final step, the model is cast into the form of Langevin equations (Pope, 2000), invoking the concept of Lagrangian fluid elements.

### S1.4.1 | Probabilistic description

We describe the droplets by the joint PDF of droplets and air,  $\mathcal{F}(\mathbf{U}, S, R^2, \mathbf{x}; t)$ , which is the probability density of the event

$$E_d : \{ \mathbf{x}_\alpha(t) = \mathbf{x}, \quad r_\alpha(t)^2 = R^2 > 0, \quad \mathbf{u}(\mathbf{x}_\alpha(t), t) = \mathbf{U}, \quad \text{and} \quad s(\mathbf{x}_\alpha(t), t) = S \} \quad (\text{S1.18})$$

for a droplet  $\alpha$ . Our definition of probability densities of events is that of Pope (1985). The PDF  $\mathcal{F}$  is *Lagrangian*, since it is a PDF evaluated along Lagrangian trajectories (Pope, 2000), the trajectories of the advected droplets. By defining  $\mathcal{F}$  as a density in squared droplet radius  $r_\alpha^2(t)$ , instead of droplet radius  $r_\alpha(t)$ , we avoid complications that follow from that  $dr_\alpha/dt$  diverges in the limit  $r_\alpha(t) \rightarrow 0$  when we formulate the evolution equation of  $\mathcal{F}$  below. Droplets that

evaporate according to Equation S1.13e may adopt a zero radius,  $r_\alpha^2(t) = 0$ . When  $r_\alpha^2(t)$  becomes zero the droplet has evaporated completely and no longer plays any role for the dynamics. Therefore only droplets with  $R^2 > 0$  are considered in  $\mathcal{F}$ . In this setup  $\mathcal{F}$  is normalised to  $1 - P_e(t)$ , reflecting that the total probability of  $\mathcal{F}$  decreases as droplets completely evaporate. The observables that we solve for are contained in  $\mathcal{F}$ . We compute the droplet-size distribution as

$$\mathcal{F}_r(R; t) = 2R \int \mathcal{F}(\mathbf{U}, S, R^2, \mathbf{x}; t) d\mathbf{U} dS d\mathbf{x}, \quad (\text{S1.19})$$

and we compute the fraction of completely evaporated droplets as

$$P_e(t) = 1 - \int \mathcal{F}(\mathbf{U}, S, R^2, \mathbf{x}; t) d\mathbf{U} dS dR^2 d\mathbf{x}. \quad (\text{S1.20})$$

The air is described by the joint PDF of velocity and supersaturation,  $f(\mathbf{U}, S; \mathbf{x}, t)$ , which is the probability density of the event

$$E_a : \{\mathbf{u}(\mathbf{x}, t) = \mathbf{U} \quad \text{and} \quad s(\mathbf{x}, t) = S\}. \quad (\text{S1.21})$$

As opposed to  $\mathcal{F}$ , the PDF  $f$  is normalised to unity at all times. Note also that  $f$  is *Eulerian*, since it is a PDF of fluid properties at a fixed position (Pope, 2000). PDF models for single-phase flows describe turbulent flows with one or several advected scalar fields (Pope, 2000). They solve for an Eulerian joint PDF of velocity and scalars. This PDF is analogous to  $f$ , but may describe more than one advected scalar field. As in some combustion problems (Stöllinger et al., 2013; Jenny et al., 2012; Haworth, 2010), we must consider a dispersed phase (the droplets) that interacts with a fluid phase (the air). As a consequence, we need two PDF:s to describe the dynamics.

Exact evolution equations of Lagrangian and Eulerian PDF:s are given in Pope (1985). To obtain the evolution equation for  $\mathcal{F}$ , we integrate a corresponding transition PDF in Pope (1985) over  $\mathcal{F}(\mathbf{U}, S, R^2, \mathbf{x}; t = 0)$ , which is known from the intial conditions. The microscopic equations S1.13 imply that the dynamics of  $\mathcal{F}$  and  $f$  read:

$$\begin{aligned} \frac{\partial \mathcal{F}}{\partial t} + U_i \frac{\partial \mathcal{F}}{\partial x_i} + \text{Da}_d S \frac{\partial \mathcal{F}}{\partial R^2} \\ = - \frac{\partial}{\partial U_i} \left\langle \frac{1}{\text{Re}_L} \nabla^2 u_i - \frac{\partial p}{\partial x_i} \middle| E_d \right\rangle \mathcal{F} - \frac{\partial}{\partial S} \left\langle \frac{1}{\text{Re}_L \text{Sc}} \nabla^2 s \middle| E_d \right\rangle \mathcal{F} - \text{Da}_s \chi V \frac{\partial}{\partial S} \left\langle \overline{r_\alpha(t) s(\mathbf{x}_\alpha, t)} \middle| E_d \right\rangle \mathcal{F}, \end{aligned} \quad (\text{S1.22a})$$

$$\frac{\partial f}{\partial t} + U_i \frac{\partial f}{\partial x_i} = - \frac{\partial}{\partial U_i} \left\langle \frac{1}{\text{Re}_L} \nabla^2 u_i - \frac{\partial p}{\partial x_i} \middle| E_a \right\rangle f - \frac{\partial}{\partial S} \left\langle \frac{1}{\text{Re}_L \text{Sc}} \nabla^2 s \middle| E_a \right\rangle f - \text{Da}_s \chi V \frac{\partial}{\partial S} \left\langle \overline{r_\alpha(t) s(\mathbf{x}_\alpha, t)} \middle| E_a \right\rangle f. \quad (\text{S1.22b})$$

Here, we follow Pope (1985) and write the components of positions and velocities by  $(x_1, x_2, x_3)$ ,  $(u_1, u_2, u_3)$  and  $(U_1, U_2, U_3)$ , and sum over repeated indices. Averages conditioned upon the events in Equations S1.18 and S1.21 are denoted by  $\langle \dots | E_d \rangle$  and  $\langle \dots | E_a \rangle$ .

We have imposed that a droplet that has evaporated completely must remain at  $r_\alpha^2(t) = 0$ . Since  $\mathcal{F}$  describes droplets with positive radii, this dynamics implies a boundary condition for  $\mathcal{F}$  at  $R^2 = 0$ , described by the probability

current (Gardiner, 2009)

$$\mathcal{J}_e(\mathbf{U}, S, \mathbf{x}; t) = \begin{cases} -\text{Da}_d S \lim_{R^2 \rightarrow 0^+} \mathcal{F}(\mathbf{U}, S, R^2, \mathbf{x}; t) & \text{if } S < 0 \\ 0 & \text{otherwise} \end{cases} \quad (\text{S1.23})$$

in the negative  $R^2$  direction. Here, the limit  $R^2 \rightarrow 0^+$  is required, since  $R^2 > 0$  in  $\mathcal{F}$ . The probability current in Equation S1.23 is non-negative,  $\mathcal{J}_e(\mathbf{U}, S, \mathbf{x}; t) \geq 0$ , which reflects that droplets can reach  $r_\alpha^2(t) = 0$  from above, but not from below. The rate of complete droplet evaporation can be written in terms of the probability current as

$$\frac{dP_e}{dt} = \int \mathcal{J}_e(\mathbf{U}, S, \mathbf{x}; t) d\mathbf{U} dS d\mathbf{x}. \quad (\text{S1.24})$$

In addition to the boundary condition at  $R^2 = 0$ ,  $\mathcal{F}$  and  $f$  inherit the spatial periodicity of the slab configuration [Figure (1b)]. The variables  $\mathbf{U}$  and  $S$  are not bounded, and require no boundary conditions. The initial conditions for  $\mathcal{F}$  and  $f$  are determined by the initial supersaturation profile (Equation S1.10 or S1.11), the initial spatial distribution of droplets, the initial droplet-size distribution, and the PDF of velocity  $\varphi(\mathbf{U}; \mathbf{x}, t)$ , which is the probability density of the event  $\mathbf{u}(\mathbf{x}, t) = \mathbf{U}$ . We discuss the PDF  $\varphi(\mathbf{U}; \mathbf{x}, t)$  below.

The evolution equations S1.22, together with their initial and boundary conditions, constitute an exact description of the dynamics of  $\mathcal{F}$  and  $f$ . The terms on the left-hand sides of Equations S1.22a and S1.22b are in closed form, as they can be computed in terms of the PDFs. The terms on the right-hand sides are not in closed form, and must be approximated in order to solve for the joint evolution of  $\mathcal{F}$  and  $f$ . They correspond to the fluctuating acceleration and diffusive flux of supersaturation that a fluid element experiences.

## S1.4.2 | Closure

We follow (Pope, 2000) and model the fluctuating acceleration of fluid elements with velocities  $\mathbf{u}(t)$  in statistically stationary, homogeneous and isotropic turbulence as a three-dimensional Ornstein-Uhlenbeck process:

$$d\mathbf{u} = -\frac{3}{4}C_0\mathbf{u}dt + \left(\frac{3}{2}C_0\right)^{\frac{1}{2}}d\boldsymbol{\eta}. \quad (\text{S1.25})$$

In this Langevin equation,  $C_0$  is a constant that depends on the Taylor-scale Reynolds number  $\text{Re}_\lambda = \sqrt{10\text{Re}_L}$  (Pope, 2011), and  $d\boldsymbol{\eta}$  is the increment of a three-dimensional isotropic Wiener process (Pope, 2000). We model the  $\text{Re}_\lambda$ -dependence of  $C_0$  according to the empirical fit of Pope (2011),  $C_0 = 6.5/(1 + 140\text{Re}_\lambda^{-4/3})^{\frac{3}{4}}$ . Equation S1.25 dictates that each velocity component of a fluid element evolves stochastically according to an independent one-dimensional Ornstein-Uhlenbeck process with dimensional variance  $2\text{TKE}/3$ . Another consequence of Equation S1.25 is that the auto-correlation function  $\rho(s) = \langle u(t)u(t+s) \rangle$  (dimensional  $t$  and  $s$ ) of the velocity component  $u(t)$  of a fluid element decays exponentially at the time-scale  $4\tau_L/(3C_0)$ . In our non-dimensional units, the Ornstein-Uhlenbeck processes have variance unity and auto-correlation time  $4/(3C_0)$ . With Equation S1.25, the PDF of fluid-element velocity relaxes to a joint normal distribution at this time scale (Pope, 2000).

The joint normal PDF of fluid-element velocity components and the exponential decay of  $\rho(s)$  dictated by Equation S1.25 is observed empirically (Pope, 2000, 2011). In the limit  $\text{Re}_\lambda \rightarrow \infty$ ,  $C_0$  approaches 6.5, a measured value for the Kolmogorov constant that specifies how the second order Lagrangian structure function depends on the Lagrangian auto-correlation time and the mean dissipation rate in high-Reynolds number turbulence (Pope, 2011). Con-

sistently with the Kolmogorov theory of turbulence (Kolmogorov, 1941), the statistics pertaining to the motion of a fluid element subject to Equation S1.25 is Reynolds-number independent at high Reynolds numbers. Equation S1.25 does not take into account that the dissipation rate experienced by a fluid element fluctuates intermittently around the mean dissipation rate  $\varepsilon$ , as predicted by Kolmogorov's refined theory of turbulence (Kolmogorov, 1962). This intermittency can be taken into account using the refined Langevin model of Pope and Chen (1990), which is an extension of Equation S1.25. Since Equation S1.25 reproduces the observed variance and autocorrelation time of fluid-element velocities, Equation S1.25 ensures that the empirically observed turbulent diffusion of passive scalars is correctly described (Pope, 2000).

Equation S1.25 for the velocity of fluid elements provides closure for the first terms on the right-hand sides of Equations S1.22a and S1.22b. The joint PDF of droplets and air  $\mathcal{F}$  is a probability density in the velocity of a fluid element, a fluid element that moves together with one of the advected droplets. The closure for Equation S1.22a therefore follows directly from Equation S1.25. The joint PDF of velocity and supersaturation  $f$  is not a probability density in the velocity of a fluid element. The closure implied for Equation S1.22b is therefore somewhat more intricate. As explained by Pope (2000), the crucial step in the derivation of this closure is to consider the relation between (the Eulerian)  $f$  and a corresponding Lagrangian PDF that is conditioned upon the initial position of a fluid element. In an incompressible flow,  $f$  is obtained by integrating this Lagrangian PDF over initial positions of fluid elements. Equation S1.25 prescribes a Fokker-Planck equation for the Lagrangian PDF. Since this Fokker-Planck equation does not depend upon the initial position of the fluid element, a Fokker-Planck equation of the same form follows for  $f$ . Following Pope (2000), we conclude that Equation S1.25 implies that the first terms on the right-hand sides of Equations S1.22a and S1.22b are given by two Fokker-Planck equations:

$$-\frac{\partial}{\partial U_i} \left\langle \frac{1}{\text{Re}_L} \nabla^2 u_i - \frac{\partial p}{\partial x_i} \middle| E_d \right\rangle \mathcal{F} = \frac{3}{4} C_0 \frac{\partial}{\partial U_i} U_i \mathcal{F} + \frac{3}{4} C_0 \frac{\partial^2 \mathcal{F}}{\partial U_i \partial U_i}, \quad \text{and} \quad (\text{S1.26a})$$

$$-\frac{\partial}{\partial U_i} \left\langle \frac{1}{\text{Re}_L} \nabla^2 u_i - \frac{\partial p}{\partial x_i} \middle| E_a \right\rangle f = \frac{3}{4} C_0 \frac{\partial}{\partial U_i} U_i f + \frac{3}{4} C_0 \frac{\partial^2 f}{\partial U_i \partial U_i}. \quad (\text{S1.26b})$$

In addition to providing closure to the first terms on the right-hand sides of Equations S1.22a and S1.22b, Equation S1.25 sets the initial conditions of  $\mathcal{F}$  and  $f$ . Statistical homogeneity and stationarity dictates that the PDF of velocity  $\varphi(\mathbf{U}; \mathbf{x}, t)$  discussed above is independent of  $\mathbf{x}$  and  $t$ . To obtain statistically stationary modeled turbulence it follows from Equation S1.25 that  $\varphi(\mathbf{U}; \mathbf{x}, t)$  must be joint normal in the velocity components.

For the second terms on the right-hand sides of Equations S1.22a and S1.22b, we make the following closure:

$$\left\langle \frac{1}{\text{Re}_L \text{Sc}} \nabla^2 s \middle| E_d \right\rangle = \left\langle \frac{1}{\text{Re}_L \text{Sc}} \nabla^2 s \middle| E_a \right\rangle = -\frac{1}{2} C_\phi (S - \langle s(\mathbf{x}, t) \rangle). \quad (\text{S1.27})$$

Here,  $C_\phi$  is an empirical constant, and  $\langle s(\mathbf{x}, t) \rangle$  is defined as the position-dependent average

$$\langle s(\mathbf{x}, t) \rangle = \int S f(\mathbf{U}, S; \mathbf{x}, t) d\mathbf{U} dS. \quad (\text{S1.28})$$

Equation S1.27 ensures that the combined effect of molecular diffusion and turbulent mixing results in the correct decay of the variance  $\text{Var}[s(\mathbf{x}, t)] = \langle s(\mathbf{x}, t)^2 \rangle - \langle s(\mathbf{x}, t) \rangle^2$  of supersaturation, at least under homogeneous conditions ( $\partial f / \partial x_i = 0$ ). Here,  $\langle s(\mathbf{x}, t)^2 \rangle$  is the mean-squared supersaturation, given by Equation S1.28 with  $S$  replaced by  $S^2$  in the integrand. Experiments and DNS support that, under homogeneous conditions, the variance of supersaturation

in fully developed turbulence decays as

$$\frac{d}{dt} \text{Var}[s(\mathbf{x}, t)] = -C_\phi \text{Var}[s(\mathbf{x}, t)], \quad (\text{S1.29})$$

with  $C_\phi \sim 2$ , independently of the molecular diffusivity (independently of  $Sc$ ) (Pope, 2000). This decay rate is reproduced by Equation S1.27. Furthermore, Equation S1.27 respects the boundedness condition of a passive scalar (Pope, 2000). This means that, in the absence of evaporation or condensation, the supersaturation remains bounded between its maximal and minimal values. Other aspects of the decay of supersaturation fluctuations may not be correctly reproduced by Equation S1.27 (Pope, 2000).

For the third terms on the right-hand sides of Equations S1.22a and S1.22b, we make the following closure:

$$\langle \overline{r_\alpha(t)s(\mathbf{x}_\alpha, t)} | E_d \rangle = \langle \overline{r_\alpha(t)s(\mathbf{x}_\alpha, t)} | E_a \rangle = \langle r(t)s(\mathbf{x}, t) \rangle, \quad (\text{S1.30})$$

where  $\langle r(t)s(\mathbf{x}, t) \rangle$  is the position-dependent average

$$\langle r(t)s(\mathbf{x}, t) \rangle = \int R S \mathcal{F}(\mathbf{U}, S, R^2, \mathbf{x}; t) d\mathbf{U} dS dR^2. \quad (\text{S1.31})$$

Equation S1.30 ensures that the liquid-water potential temperature analogue  $\theta$  is conserved under the statistical model. With this closure we replace the local average  $\overline{r_\alpha(t)s(\mathbf{x}_\alpha, t)}$ , which describes local neighborhoods of droplets, by  $\langle r(t)s(\mathbf{x}, t) \rangle$ , which is an expectation for a single droplet. As a consequence, the self-limiting nature of droplet evaporation may not be accurately described by the statistical model. To model local conditional averages as in Equation S1.30 is a standard way to obtain closure for PDF models that describe combustion of particles in turbulence (Jenny et al., 2012; Stöllinger et al., 2013; Haworth, 2010).

Inserting Equations S1.26, S1.27 and S1.30 into Equations S1.22, we obtain a model for the joint evolution of  $\mathcal{F}$  and  $f$ :

$$\begin{aligned} \frac{\partial \mathcal{F}}{\partial t} + U_i \frac{\partial \mathcal{F}}{\partial x_i} + 2Da_d S \frac{\partial \mathcal{F}}{\partial R^2} \\ = \frac{3}{4} C_0 \frac{\partial}{\partial U_i} U_i \mathcal{F} + \frac{3}{4} C_0 \frac{\partial^2 \mathcal{F}}{\partial U_i \partial U_i} + \frac{1}{2} C_\phi \frac{\partial}{\partial S} (S - \langle s(\mathbf{x}, t) \rangle) \mathcal{F} - Da_s \chi V \frac{\partial}{\partial S} \langle r(t)s(\mathbf{x}, t) \rangle \mathcal{F}, \end{aligned} \quad (\text{S1.32a})$$

$$\frac{\partial f}{\partial t} + U_i \frac{\partial f}{\partial x_i} = \frac{3}{4} C_0 \frac{\partial}{\partial U_i} U_i f + \frac{3}{4} C_0 \frac{\partial^2 f}{\partial U_i \partial U_i} + \frac{1}{2} C_\phi \frac{\partial}{\partial S} (S - \langle s(\mathbf{x}, t) \rangle) f - Da_s \chi V \frac{\partial}{\partial S} \langle r(t)s(\mathbf{x}, t) \rangle f. \quad (\text{S1.32b})$$

These equations are the statistical model, described as a closed set of evolution equations for  $\mathcal{F}$  and  $f$ . We note that  $\mathcal{F}$  and  $f$  couple to each other through the averages  $\langle s(\mathbf{x}, t) \rangle$  and  $\langle r(t)s(\mathbf{x}, t) \rangle$ . This coupling is a consequence of that droplets are affected by the supersaturation of the air, and that the supersaturation of the air is affected by evaporating droplets.

### S1.4.3 | Lagrangian dynamics

The PDF dynamics in Equations S1.32 can be cast into a set of equations that describe the dynamics of Lagrangian fluid elements (Pope, 2011). The dynamics of Lagrangian fluid elements with positions  $\mathbf{x}(t)$ , velocities  $\mathbf{u}(t)$ , and

supersaturations  $s(t)$  that corresponds to Equation S1.32b is given by Equation S1.25, together with:

$$\frac{d\mathbf{x}}{dt} = \mathbf{u}, \quad (\text{S1.33a})$$

$$\frac{ds}{dt} = -\frac{1}{2}C_\phi (s - \langle s(\mathbf{x}, t) \rangle) - \text{Da}_s \chi V \langle r(t)s(\mathbf{x}, t) \rangle. \quad (\text{S1.33b})$$

Since droplets are advected, they move together with Lagrangian fluid elements. Therefore, some Lagrangian fluid elements coincide with droplets. We describe such fluid elements by the radii  $r(t)$  of the droplets that they coincide with, in addition to their positions, velocities and supersaturations. Their dynamics corresponds to Equation S1.32a, and is given by Equations S1.25 and S1.33, together with

$$\frac{dr^2}{dt} = \begin{cases} \text{Da}_d s & \text{if } r^2(t) > 0 \\ 0 & \text{if } r^2(t) = 0 \end{cases}. \quad (\text{S1.34})$$

The relations between fluid-element dynamics and evolution equations of Eulerian and Lagrangian PDF:s are derived by Pope (1985). To conclude why Equations S1.25, S1.33, and S1.34 correspond to Equations S1.32, we give a brief summary of the derivations for our statistical-model dynamics. First, one recognises that fluid elements with droplets sample  $\mathcal{F}$ , and that fluid elements without droplets sample  $f$ . Second, one formulates the Fokker-Planck equations for the two types of fluid elements. The Fokker-Planck equation for fluid elements with droplets is Equation S1.32a, subject to the boundary condition S1.23. To obtain Equation S1.32b from the fluid elements without droplets, one integrates their Fokker-Planck equation over initial positions. Equation S1.32b then follows, as a consequence of the relation between Lagrangian and Eulerian PDF:s mentioned above.

#### S1.4.4 | Computation of observables and statistical one-dimensionality

Since the PDF dynamics of our statistical model is implied by the dynamics of Lagrangian fluid elements, we solve Equations S1.32 for the PDF:s by evolving fluid elements according to Equations S1.25, S1.33 and S1.34. The averages  $\langle s(\mathbf{x}, t) \rangle$  and  $\langle r(t)s(\mathbf{x}, t) \rangle$  are known in terms of the fluid elements, since the fluid elements sample  $\mathcal{F}$  and  $f$ . In practice, these averages are computed using kernel estimates, as described by Pope (2000). Since  $\langle s(\mathbf{x}, t) \rangle$  and  $\langle r(t)s(\mathbf{x}, t) \rangle$  are known, Equations S1.25, S1.33 and S1.34 form a closed set of equations that govern the simultaneous evolution of an ensemble of fluid elements. Since fluid elements with droplets sample  $\mathcal{F}$ , we can compute the droplet-size distribution and the fraction of completely evaporated droplets from them according to Equations S1.19 and S1.20.

To compute our results, we use the one-dimensional form of the statistical model shown in the main text. This is possible, since the dynamics that we model is statistically one-dimensional. Statistical one-dimensionality follows from that the turbulence is statistically homogeneous and isotropic, and from that our initial conditions are one-dimensional. The direction of statistical inhomogeneity is  $x$ . The PDF:s  $\mathcal{F}(\mathbf{U}, S, R^2, \mathbf{x}; t)$  and  $f(\mathbf{U}, S; \mathbf{x}, t)$ , as well as the averages  $\langle r(t)s(\mathbf{x}, t) \rangle$  and  $\langle s(\mathbf{x}, t) \rangle$  that they form, depend on the three-dimensional position  $\mathbf{x}$  only through  $x$ . As explained by Pope (1985), it is therefore sufficient to evolve only the  $x$ -components of fluid element positions and velocities. In the main text, we have taken the statistical one-dimensionality into account and replaced  $\langle r(t)s(\mathbf{x}, t) \rangle$  and  $\langle s(\mathbf{x}, t) \rangle$  by  $\langle r(t)s(x, t) \rangle$  and  $\langle s(x, t) \rangle$ .

### S1.4.5 | Averaging

The mean cubed radius of droplets and the volume average of supersaturation are required to compute the liquid-water potential temperature analogue  $\theta$ . In the statistical model the mean cubed radius of droplets is given by:

$$\langle r(t)^3 \rangle = \frac{1}{1 - P_e(t)} \int R^3 \mathcal{F}(\mathbf{U}, S, R^2, \mathbf{x}; t) d\mathbf{U} dS dR^2 d\mathbf{x}. \quad (\text{S1.35})$$

The volume average of supersaturation is given by:

$$\langle s(t) \rangle = \frac{1}{V} \int S f(\mathbf{U}, S; \mathbf{x}, t) d\mathbf{U} dS d\mathbf{x}. \quad (\text{S1.36})$$

## S1.5 | SIMULATION PARAMETERS

The parameters of our simulations are listed in Table S1. The parameters for Figures 2 to 4 are taken from the DNS of Kumar et al. (2012, 2014, 2018). The results of (Kumar et al., 2014, 2018) and Andrejczuk et al. (2006) shown in these figures are not obtained using Equations 1, the microscopic equations that we model. The interpretation of the simulation setups of Kumar et al. (2014, 2018) and Andrejczuk et al. (2006) in terms of our parameters is discussed in Sections S1.1 and S1.7. Kumar et al. (2018) did not give their values of  $\zeta_1$ ,  $\zeta_2$ , and  $s_c$ , but we obtained them through private communication (Kumar, 2019). For Figure 4, we use the values of  $C_0$  and  $L$  of Run 5 of Kumar et al. (2018), since we wanted to compare with DNS and are interested in large-Reynolds number regimes. All simulations use  $C_\phi = 2$ , a common estimate for this empirical parameter (Pope, 2000).

In Figure 5 we analyse measurements from the top panel of Figure 3 of Beals et al. (2015). In the supplemental material of that paper, the authors show droplet-size distributions and droplet-number densities of the undiluted cloud air. The distribution of droplet radii that we use to analyse the top panel in Figure 3 of Beals et al. (2015) is very close to Gaussian, as explained in Section S1.8. For our Figure 5, we fit a Gaussian to this distribution, and the fit is parameterised by the non-dimensional standard deviation  $\sigma_0 = 0.1386$ . We also use  $C_0 = 6.5$  and  $L = 2.28$  for Figure 5. This value of  $L$  is an estimate of the constant of proportionality between the dimensional domain size and  $U\tau_L$  at large Reynolds numbers. We compute this estimate by in two steps. First, we estimate the turbulent kinetic energy associated to a spatial scale  $\ell$  by integrating the energy-spectrum function (Pope, 2000) from the wave number  $k = 2\pi/\ell$ :

$$\text{TKE} = \int_{2\pi/\ell}^{\infty} C \varepsilon^{\frac{2}{3}} k^{-\frac{5}{3}} dk = C \frac{3}{2} \left( \frac{\varepsilon \ell}{2\pi} \right)^{\frac{2}{3}}. \quad (\text{S1.37})$$

Here,  $C$  is a Kolmogorov constant that has been measured to  $C = 1.5$  (Pope, 2000). Second, we use this value of the Kolmogorov constant and find

$$\frac{\ell}{U\tau_L} = \frac{4\pi}{3} C^{-\frac{3}{2}} = 2.28. \quad (\text{S1.38})$$

Since 2.28 is the constant of proportionality between an arbitrary spatial scale and  $U\tau_L$ , it is the constant of proportionality between the dimensional domain size and  $U\tau_L$ . We therefore conclude that our estimate in Equation S1.37 gives  $L = 2.28$  and  $V = L^3 = 11.85$ .

Table S1 provides a set of independent parameters that, together with  $C_\phi = 2$ , specify our simulations. Also



shown are a few dependent parameters. These include the Damköhler number ratio  $\mathcal{R} = \text{Da}_d/\text{Da}_s$  and the critical Damköhler number ratio

$$\mathcal{R}_c = -\frac{2}{3} \frac{\chi}{\langle s(0) \rangle}, \quad (\text{S1.39})$$

where  $\langle s(0) \rangle$  is the initial volume average of the supersaturation (defined below). Also included is the coefficient  $\chi_0$  that determine  $\langle s(0) \rangle$  together with  $\chi$  and  $s_c$ . The initial volume average of the supersaturation can be written

$$\langle s(0) \rangle = (1 + s_c)(\chi + \chi_0) - 1, \quad (\text{S1.40})$$

a replacement that is done in the main text. For Figure 5, we have  $\chi_0 = s_c = 0$ , so  $\langle s(0) \rangle = \chi - 1$ . For Figures 2 to 4, we have a non-zero  $\chi_0$ , since the initial supersaturation profile is smooth. Here, the parameters  $\zeta_1$  and  $\zeta_2$  that determine the initial supersaturation profile are tied to specific values of  $\chi$ . It is only for these values of  $\chi$  that the initial supersaturation is approximately zero at  $x = \pm\chi L/2$ , the edges of the cloud slab [Figure 1(b)]. For a general  $\chi$ , the volume average of the initial supersaturation is given by Equation S1.40, with a value of  $\chi_0$  that can be computed from  $\zeta_1$ ,  $\zeta_2$ , and  $s_c$ .

## S1.6 | NUMERICS

We solve the statistical model using computer simulations that evolve an ensemble of Lagrangian fluid elements according to Equations 3. Fluid elements with droplets are initialised uniformly over the interval  $-\chi L/2 < x < \chi L/2$ . To ensure that  $\langle s(x, t) \rangle$  can be computed in the whole simulation domain, we initialise fluid elements without droplets uniformly over  $-L/2 < x < L/2$  (Pope, 2000). We solve for the supersaturation  $s(t)$  and squared radius  $r^2(t)$  of fluid elements using Euler's method (Rade and Westergren, 2013). We use a dynamical time step that ensures that the absolute errors in  $s(t)$  and  $r^2(t)$  at each time step are smaller than a given threshold. At each time step, the position  $x(t)$  and velocity  $u(t)$  of a fluid element are drawn from their exact joint distribution, which is conditioned on the position and velocity before the time step (Gillespie, 1996). The averages  $\langle s(x, t) \rangle$  and  $\langle r(t)s(x, t) \rangle$  are computed from the fluid elements on a regular mesh. We obtain the mean-field values at the positions of fluid elements by linear interpolation. The spatial variations of these averages reduce with time due to mixing, and we increase the computational efficiency of our simulations by neglecting these spatial variations when they become very small. That  $\langle s(x, t) \rangle$  and  $\langle r(t)s(x, t) \rangle$  become essentially independent of  $x$  does not mean that the simulated system becomes spatially uniform. In particular, individual realisations of the simulated system may still exhibit supersaturation fluctuations that affect the evaporation of droplets for some time.

Figures 2 and 3 show droplet-size distributions and time series of  $P_e(t)$  for three simulations. To conclude convergence for these simulations, we simply check that the results do not change as we vary the parameters and thresholds that control the numerics. Figures 4 and 5 show results from hundreds of simulations. To address the convergence of these simulations, we test the accuracy of our simulations for representative initial conditions and representative combinations of  $\text{Da}_d$ ,  $\mathcal{R}$  and  $\chi$ . In each test, we vary the numerical parameters separately to exclude systematical errors. To estimate the statistical errors, we compute several independent realisations for each combination of the numerical parameters. These tests allow us to conclude that no systematical errors pertain to the results in Figures 4 and 5, and that the values of  $P_e^*$  that we compute have relative errors that are less than 5 %, and/or absolute errors that are smaller than  $10^{-3}$ . The simulation results in Figures 4 and 5 are either  $P_e^*$  or functions of  $P_e^*$ , and we conclude that

none of our conclusions in the main text are affected by numerical errors.

## S1.7 | PARAMETERS OF DNS IN FIGURE 4

To place DNS of Andrejczuk et al. (2006); Kumar et al. (2012, 2013, 2014, 2018) in our phase diagram (Figure 4), we extract their dimensional parameters that determine  $Da_d$  and  $\mathcal{R}/\mathcal{R}_c$ . The computed values are listed in Table S2 for Kumar et al. (2012, 2013, 2014, 2018), and in Table S3 for Andrejczuk et al. (2006).

### S1.7.1 | DNS of Kumar et al. (2012, 2013, 2014, 2018)

It is straightforward to compute  $Da_d$ ,  $\mathcal{R}$ , and  $\mathcal{R}_c$  for the simulations in Kumar et al. (2012, 2013, 2018) and three simulations in Kumar et al. (2014), since they are for stationary turbulence with Lagrangian droplets, just as Equations 1. First, one casts the dynamics into the dynamics of Equations S1.1, using the simplifications described in Section S1.1. After that one non-dimensionalise as described in Section S1.3. The simulations of Kumar et al. (2012, 2013, 2014, 2018) shown in Figure 4 are the simulations for which one can conclude if  $P_e^* > 10\%$  or if  $P_e^* < 10\%$ .

### S1.7.2 | DNS of Andrejczuk et al. (2006)

Figure 4 shows 42 simulations of Andrejczuk et al. (2006). Andrejczuk et al. (2006) reports of 58 simulations, but we can only read off whether  $P_e^* > 10\%$  or not for 50 of them. Out of these 50 simulations, eight simulations fall outside the plot range of Figure 4. We therefore show 42 simulations of Andrejczuk et al. (2006) in Figure 4.

The simulations of Andrejczuk et al. (2006) are for decaying turbulence and initial conditions in the form of randomly distributed cloudy filaments in dry air. The parameter  $Da_d$  in Equation S1.15 is defined for the stationary turbulence and the initial conditions of our simulations, so it has no direct counterpart in Andrejczuk et al. (2006). To nevertheless discuss the simulations of Andrejczuk et al. (2006) we compute a time-scale ratio that incorporates the same physics as  $Da_d$ . We then place a simulation in Figure 4 by assuming that this time-scale ratio is equal to  $Da_d$ . The time-scale ratio is computed as  $Da_d = \tau_L/\tau_d$ , but with  $\tau_L$  taken as  $TKE/\varepsilon$  at the time when TKE decayed fastest in Andrejczuk et al. (2006). We estimate these values of TKE and  $\varepsilon$  from plots in Andrejczuk et al. (2006).

The coefficient  $A_3$  enters the dynamics multiplied by an unnamed factor  $\gamma_{A_3}$  in Andrejczuk et al. (2006), and we read off  $A_3/\gamma_{A_3} = 10^{-10}$  m<sup>2</sup>/s. We extract the density  $\varrho_a$  of air and the density  $\varrho_w$  of pure liquid water Andrejczuk et al. (2006, 2004). The expression for saturation pressure of water vapour is not given in Andrejczuk et al. (2006), so we can not compute their value of  $A_2$  using Equation S1.9. We therefore use the value  $A_2 = 413$  m<sup>3</sup>/kg that we compute for Kumar et al. (2014). To nevertheless analyse DNS results of Andrejczuk et al. (2006) qualitatively is justified since the temperatures and water-vapour densities in Andrejczuk et al. (2006) and Kumar et al. (2014) imply that their values of  $A_2$  are similar. We compute  $s_e$  as one minus the relative humidity of the non-cloudy initial filaments, which we extract from tables in Andrejczuk et al. (2006). We also extract the volume fraction  $\chi$  of cloudy air, and the liquid-water mixing ratio  $q_\ell$  of the initially cloudy filaments from these tables. We interpret the initially cloudy filaments as saturated and possessing sharp edges, even though this is not stated explicitly in Andrejczuk et al. (2006), so that  $\mathcal{R}_c = -2\chi/[3(\chi - 1)]$ .

Andrejczuk et al. (2006) do not use Lagrangian droplets. Instead, they employ a field description in which droplets are binned into 16 size categories. The three initially populated bins are centered at droplet radii 8, 8.75, and 9.5  $\mu$ m, and they contained 25%, 50%, and 25% of the liquid-water mixing ratio  $q_\ell$ . We compute the number density of

droplets within a bin centered at the droplet radius  $r$  that contains a fraction  $\xi_r$  of liquid-water mixing ratio as  $n_r = 3\xi_r q_{\ell} \varrho_a / (4\pi r^3 \varrho_w)$ . By summing up the number densities for  $r = 8, 8.75$ , and  $9.5 \mu\text{m}$ , we find the droplet-number density  $n_0$  of the initially cloudy filaments. We compute the initial volume radii of droplets as  $r_0 = [3q_{\ell} \varrho_a / (4\pi n_0 \varrho_w)]^{1/3}$

## S1.8 | ESTIMATES USED TO ANALYSE DATA FROM Beals et al. (2015)

The black crosses in Figure 5(a) are from the top panel of Figure 3 of Beals et al. (2015), and represent droplets measured during a research flight through a convective cloud. Droplet-size distributions and thermodynamic conditions are not given for this flight, so we estimate them using data from a typical flight detailed in the supplementary materials of Beals et al. (2015), namely pass 2 of the research flight RF05.

To estimate the parameters of our model, we need actual values for physical coefficients. We use  $\Lambda = 2.5 \cdot 10^6 \text{ J/kg}$ ,  $c_p = 1005 \text{ J/(kg}\cdot\text{K)}$ , and  $R_v = 461.5 \text{ J/(kg}\cdot\text{K)}$  from Rogers and Yau (1989). We also set the density of pure liquid water to  $\varrho_w = 1000 \text{ kg/m}^3$ . Figure S3 of Beals et al. (2015) shows that pass 2 of RF05 traverses a cloud at a constant altitude of 4000 m. We therefore assume the pressure of the International Standard Atmosphere (Cavcar, 2000) at this altitude,  $p \sim 62000 \text{ Pa}$ . The precise value of the pressure is not important, since conclusions that rely on the estimates in this Section are unchanged if we assume a pressure that is 10 % lower or higher. We extract  $K_a$  and  $D_v$  at our assumed pressure from Table 7.1 of Rogers and Yau (1989). Furthermore, we assume that the saturation pressure of water vapour is given by Equation (2.12) in Rogers and Yau (1989). We also use the relation between potential temperature  $\Theta$ , temperature  $T$ , and pressure  $p$  of Rogers and Yau (1989),  $\Theta = T (10^5 \text{ Pa}/p)^{0.286}$ .

The droplet-size distribution of undiluted cloud air traversed during pass 2 of RF05 is shown in Figure S7 of Beals et al. (2015). The distribution of droplet radii is very close Gaussian, normalised to the number-density of droplets. We make a Gaussian fit with mean  $4.42 \mu\text{m}$ , and standard deviation  $0.626 \mu\text{m}$ . The corresponding volume radius is  $r_0 = 4.51 \mu\text{m}$ , which gives the non-dimensional standard deviation  $\sigma_0 = 0.1386$ . We use this value of  $\sigma_0$  to parameterise the initial droplet-size distribution in the statistical-model simulations shown in Figure 5. The normalisation of the Gaussian fit gives the droplet-number density  $n_0 = 764 \text{ cm}^{-3}$ . We compute the liquid-water density of the undiluted cloud as  $\varrho_{\ell c} = (4\pi r_0^3/3) n_0 \varrho_w = 2.94 \cdot 10^{-4} \text{ kg/m}^3$ . This value of  $\varrho_{\ell c}$  is consistent with the liquid-water density plot in Figure S4 of Beals et al. (2015).

We estimate temperatures from the liquid-water potential temperature shown in Figure S4 of Beals et al. (2015). Here, the liquid-water potential temperature varies between  $\Theta_{\ell c} = 294.8 \text{ K}$  within the cloud and  $\Theta_{\ell e} = 295.8 \text{ K}$  outside the cloud. The liquid-water potential temperature is the same as the potential temperature  $\Theta_e$  outside the cloud,  $\Theta_e = 295.8 \text{ K}$ . We compute the temperature  $T_e \sim 257.6$  outside the cloud, using  $\Theta_e$  and the pressure of the International Standard Atmosphere (Cavcar, 2000). We estimate the density of dry air as  $\varrho_a = p/(R_v T_e) \sim 0.52 \text{ kg/m}^3$ . This density gives the liquid-water mixing ratio  $q_{\ell c} = \varrho_{\ell c}/\varrho_a \sim 5.6 \cdot 10^{-4}$  within the cloud. The potential temperature within the cloud can now be estimated as  $\Theta_c = \Theta_{\ell c} + (\Lambda/c_p) q_{\ell c} \sim 296.2 \text{ K}$  (Lamb and Verlinde, 2011), and the corresponding temperature estimate is  $T_c \sim 257.9 \text{ K}$ . It is seen in Figure S4 of Beals et al. (2015) that the supersaturation within the cloud is smaller than  $\sim 2\%$  in magnitude. Assuming saturation within the cloud, the estimate  $T_c \sim 257.9 \text{ K}$  gives the water-vapour mixing ratio  $q_{vc} = e_{vs}(T_c)/(\varrho_a R_v T_c) \sim 3.1 \cdot 10^{-3}$ . We extract the (negative) supersaturation  $s_e \sim -0.08$  from Figure S4 of Beals et al. (2015), and estimate the water-vapour mixing ratio outside the cloud,  $q_{ve} = e_{vs}(T_e)(s_e + 1)/(\varrho_a R_v T_e) \sim 2.7 \cdot 10^{-3}$ .

In our analysis of empirical data from Beals et al. (2015) we estimate  $\tau_s \sim 1 \text{ s}$  based on our estimates of  $T_c$ ,  $q_{vc}$ , and  $p$ . Equation S1.9 gives  $A_2 \sim 1000 \text{ m}^3/\text{kg}$  when linearising the supersaturation around the temperature  $T_c \sim 257.9 \text{ K}$  and the water-vapour mixing ratio  $q_{vc} \sim 3.1 \cdot 10^{-3}$ . We compute  $A_3 \sim 2 \cdot 10^{-11} \text{ m}^2/\text{s}$  at the pressure  $p = 62000 \text{ Pa}$  and

temperature  $T_c \sim 257.9$  K using Equation S1.7. Using the volume radius  $r_0$  and droplet-number density  $n_0$  estimated above, we find  $\tau_s \sim 1$  s using Equation S1.16.

# Table S1

TABLE S1 Simulation parameters. Our statistical-model simulations are completely specified by the two Damköhler numbers  $Da_d$  and  $Da_s$ , the constant  $C_0$  that regulates the auto-correlation time of fluid elements, the domain size  $L$ , the volume fraction  $\chi$  of cloudy air, the constants  $\zeta_1$  and  $\zeta_2$  that determine the shape of the initial supersaturation profile in Figures 2 to 4, and the supersaturation  $s_c$  at the center of the initial cloud slab, together with the empirical constant  $C_\phi = 2$ . From these parameters, we compute the Damköhler number ratio  $\mathcal{R}$ , the critical Damköhler number ratio  $\mathcal{R}_c$ , and the contribution  $\chi_0$  to the initial volume average of the supersaturation from the shape of the initial supersaturation profile.

Simulation	Independent parameters									Dependent parameters		
	$Da_d$	$Da_s$	$C_0$	$L$	$\chi$	$\sigma_0$	$\zeta_1$	$\zeta_2$	$s_c$	$\mathcal{R}$	$\mathcal{R}_c$	$\chi_0$
Figures 2 and 3, dry	2.44	0.968	5.22	2.96	0.428	0	4722	8	0.021	2.52	0.859	0.226
Figure 2, moist	1.09	1.433	5.22	2.96	0.428	0	4722	8	0.021	0.760	0.859	0.226
Figure 3, very moist	0.754	8.2	4.50	2.99	0.4	0	1410	6	0.1	0.092	0.683	0.154
Figure 4	$5E^{-3}$ - $4E^2$	$1E^{-3}$ - $9E^3$	6.09	2.66	0.429	0	690	6	0.1	$5E^{-2}$ - $4E^0$	0.913	0.195
Figure 5(a)	$1E^{-2}$ - $1E^3$	$6E^{-2}$ - $6E^3$	6.5	2.28	0.2-0.8	0.1386			0	0.17	0.17-2.7	0
Figure 5(b)	$1E^{-2}$ - $1E^3$	$3E^{-1}$ - $4E^4$	6.5	2.28	0.369-0.374	0.1386			0	$2E^{-2}$ - $3E^{-2}$	0.38-0.41	0

# Table S2

TABLE S2 Same as Table 2, but separately for each DNS from Kumar et al. (2012, 2013, 2014, 2018) in Figure 4. Non-dimensional parameters: Damköhler number  $Da_d$ , Damköhler-number ratio  $\mathcal{R}$ , critical ratio  $\mathcal{R}_c$ , and volume fraction  $\chi$  of cloudy air. Dimensional parameters: domain size  $L$ , mean dissipation rate  $\varepsilon$ , and droplet-number density  $n_0$  of the initially cloudy air.

Reference	Non-dimensional parameters					Dimensional parameters		
	$Da_d$	$Da_s$	$\mathcal{R}$	$\mathcal{R}_c$	$\chi$	$L$ [cm]	$\varepsilon$ [cm <sup>2</sup> /s <sup>3</sup> ]	$n_0$ [cm <sup>-3</sup> ]
Table 2 in Kumar et al. (2012), Row 1	0.0075	0.0820	0.0916	0.6829		25.6	33.8	164
Table 2 in Kumar et al. (2012), Row 2	0.0751	0.8204	0.0916	0.6829		25.6	33.8	164
Table 2 in Kumar et al. (2012), Row 3	0.7511	8.2041	0.0916	0.6829		25.6	33.8	164
Table 2 in Kumar et al. (2013), Row 3	0.3065	0.4185	0.7324	0.6829		25.6	33.8	164
Table 2 in Kumar et al. (2013), Row 7	0.1362	0.6277	0.2170	0.6829		25.6	33.8	164
Simulation S1 in Kumar et al. (2014)	2.4320	0.9660	2.5177	0.8377		51.2	33.8	153
Simulation S2 in Kumar et al. (2014)	1.0809	1.4490	0.7460	0.8377		51.2	33.8	153
Simulation S3 in Kumar et al. (2014)	0.6080	1.9319	0.3147	0.8377		51.2	33.8	153
Run 1 in Kumar et al. (2018)	0.1191	0.5185	0.2296	0.9150		12.8	31.9	118
Run 2 in Kumar et al. (2018)	0.1914	0.8333	0.2297	0.9155		25.6	34.6	118
Run 3 in Kumar et al. (2018)	0.3227	1.4042	0.2298	0.9163		51.2	34.7	118
Run 4 in Kumar et al. (2018)	0.5842	2.4509	0.2384	0.9503		102.4	32.1	113
Run 5 in Kumar et al. (2018)	0.9122	4.0429	0.2256	0.9000		204.8	33.6	120

## Table S3

TABLE S3 Same as Table 2, but separately for each DNS from Andrejczuk et al. (2006) in Figure 4.

Non-dimensional parameters: Damköhler number  $Da_d$ , Damköhler-number ratio  $\mathcal{R}$ , critical ratio  $\mathcal{R}_c$ , and volume fraction  $\chi$  of cloudy air. Dimensional parameters: domain size  $L$ , mean dissipation rate  $\varepsilon$ , and droplet-number density  $n_0$  of the initially cloudy air.

#	Non-dimensional parameters					Dimensional parameters		
	$Da_d$	$Da_s$	$\mathcal{R}$	$\mathcal{R}_c$	$\chi$	$L$ [cm]	$\varepsilon$ [cm <sup>2</sup> /s <sup>3</sup> ]	$n_0$ [cm <sup>-3</sup> ]
S2a <sub>1</sub>	13.7874	78.1243	0.1765	0.0996	0.13	64	1.5	1166
S2a <sub>2</sub>	6.1722	34.9739	0.1765	0.3284	0.33	64	3	1166
S2a <sub>3</sub>	12.1003	68.5642	0.1765	0.5029	0.43	64	1.7	1166
S2a <sub>4</sub>	9.6240	54.5331	0.1765	0.6667	0.5	64	1.7	1166
S2a <sub>5</sub>	10.1375	57.4425	0.1765	1.3535	0.67	64	1.5	1166
S2b <sub>1</sub>	4.3101	24.4223	0.1765	0.0996	0.13	64	8.1	1166
S2b <sub>2</sub>	4.3101	24.4223	0.1765	0.3284	0.33	64	8.1	1166
S2b <sub>3</sub>	4.3101	24.4223	0.1765	0.5029	0.43	64	8.1	1166
S2b <sub>4</sub>	4.3101	24.4223	0.1765	0.6667	0.5	64	8.1	1166
S2b <sub>5</sub>	4.3101	24.4223	0.1765	1.3535	0.67	64	8.1	1166
S2c <sub>1</sub>	0.8232	4.6646	0.1765	0.0996	0.13	64	935.3	1166
S2c <sub>2</sub>	0.8232	4.6646	0.1765	0.3284	0.33	64	935.3	1166
S2c <sub>3</sub>	0.8232	4.6646	0.1765	0.6667	0.5	64	935.3	1166
S3a <sub>2</sub>	8.2897	7.3394	1.1295	0.6667	0.5	64	1.3	182
S3a <sub>3</sub>	11.6711	20.6664	0.5647	0.6667	0.5	64	0.9	364
S3a <sub>4</sub>	9.7721	25.9556	0.3765	0.6667	0.5	64	1.4	547
S3a <sub>5</sub>	8.4295	47.7646	0.1765	0.6667	0.5	64	2	1166
S4a <sub>1</sub>	18.0709	47.9980	0.3765	0.0996	0.13	64	0.5	547
S4a <sub>2</sub>	7.3957	19.6436	0.3765	0.3284	0.33	64	1.6	547
S4a <sub>3</sub>	8.4955	22.5650	0.3765	0.5029	0.43	64	1.5	547
S4a <sub>4</sub>	9.7754	25.9643	0.3765	0.6667	0.5	64	1.3	547
S4a <sub>5</sub>	12.6777	33.6732	0.3765	1.3535	0.67	64	1.3	547
S4b <sub>2</sub>	14.1203	12.5016	1.1295	0.3284	0.33	64	0.4	182
S4b <sub>3</sub>	13.1643	11.6552	1.1295	0.5029	0.43	64	0.6	182
S4b <sub>4</sub>	8.1755	7.2383	1.1295	0.6667	0.5	64	1.1	182
S4b <sub>5</sub>	9.8085	8.6841	1.1295	1.3535	0.67	64	1.2	182
S4b <sub>6</sub>	13.9764	12.3742	1.1295	4.4615	0.87	64	0.9	182
S4c <sub>5</sub>	9.6947	3.4333	2.8237	1.3535	0.67	64	1	73
S4c <sub>6</sub>	16.1282	5.7117	2.8237	4.4615	0.87	64	0.6	73
S5a <sub>1</sub>	12.0940	34.2643	0.3530	0.6667	0.5	64	3.7	1166
S5a <sub>2</sub>	11.6186	41.8950	0.2773	0.6667	0.5	64	3.1	1166
S5a <sub>3</sub>	9.3465	52.9606	0.1765	0.6667	0.5	64	1.7	1166
S5a <sub>4</sub>	7.7943	61.8316	0.1261	0.6667	0.5	64	1.1	1166
S6a <sub>1</sub>	13.3405	37.7959	0.3530	0.6667	0.5	64	2.7	1166
S6a <sub>2</sub>	14.7497	41.7886	0.3530	0.6667	0.5	64	3.4	1166
S6a <sub>3</sub>	12.8279	36.3436	0.3530	0.6667	0.5	64	5.9	1166
S6a <sub>4</sub>	10.1435	28.7383	0.3530	0.6667	0.5	64	10.2	1166
S6b <sub>1</sub>	1.6879	4.7821	0.3530	0.6667	0.5	64	3	1166
S6b <sub>2</sub>	3.5983	10.1947	0.3530	0.6667	0.5	64	3.1	1166
S6b <sub>3</sub>	13.1067	37.1334	0.3530	0.6667	0.5	64	3.8	1166
S6b <sub>4</sub>	56.6502	160.4998	0.3530	0.6667	0.5	64	3.4	1166
S6b <sub>5</sub>	97.6054	276.5329	0.3530	0.6667	0.5	64	4.7	1166

# SI References

- Andrejczuk, M., Grabowski, W. W., Malinowski, S. P. and Smolarkiewicz, P. K. (2004) Numerical simulation of cloud–clear air interfacial mixing. *Journal of the atmospheric sciences*, **61**, 1726–1739.
- (2006) Numerical simulation of cloud–clear air interfacial mixing: Effects on cloud microphysics. *Journal of the Atmospheric Sciences*, **63**, 3204–3225.
- (2009) Numerical simulation of cloud–clear air interfacial mixing: Homogeneous versus inhomogeneous mixing. *Journal of the Atmospheric Sciences*, **66**, 2493–2500.
- Bannon, P. R. (1996) On the anelastic approximation for a compressible atmosphere. *Journal of the Atmospheric Sciences*, **53**, 3618–3628.
- Beals, M. J., Fugal, J. P., Shaw, R. A., Lu, J., Spuler, S. M. and Stith, J. L. (2015) Holographic measurements of inhomogeneous cloud mixing at the centimeter scale. *Science*, **350**, 87–90.
- Cavcar, M. (2000) The international standard atmosphere (ISA). *Anadolu University, Turkey*, **30**, 1–6.
- Devenish, B. J., Furtado, K. and Thomson, D. J. (2016) Analytical solutions of the supersaturation equation for a warm cloud. *Journal of the Atmospheric Sciences*, **73**, 3453–3465.
- Dougherty, J. P. (1961) The anisotropy of turbulence at the meteor level. *Journal of Atmospheric and Terrestrial Physics*, **21**, 210–213.
- Gardiner, C. (2009) *Stochastic Methods*, vol. 4. Springer Berlin.
- Gillespie, D. T. (1996) Exact numerical simulation of the Ornstein-Uhlenbeck process and its integral. *Physical Review E*, **54**, 2084–2091.
- Grabowski, W. W. (1993) Cumulus entrainment, fine-scale mixing, and buoyancy reversal. *Quarterly Journal of the Royal Meteorological Society*, **119**, 935–956.
- Grachev, A. A., Andreas, E. L., Fairall, C. W., Guest, P. S. and Persson, P. O. G. (2015) Similarity theory based on the Dougherty–Ozmidov length scale. *Quarterly Journal of the Royal Meteorological Society*, **141**, 1845–1856.
- Gustavsson, K. and Mehlig, B. (2016) Statistical models for spatial patterns of heavy particles in turbulence. *Advances in Physics*, **65**, 1–57.
- Gustavsson, K., Vajedi, S. and Mehlig, B. (2014) Clustering of particles falling in a turbulent flow. *Physical Review Letters*, **112**, 214501.
- Haworth, D. C. (2010) Progress in probability density function methods for turbulent reacting flows. *Progress in Energy and Combustion Science*, **36**, 168–259.
- Jeffery, C. A. (2007) Inhomogeneous cloud evaporation, invariance, and Damköhler number. *J. Geophys. Res.*, **112**, D24S21.
- Jenny, P., Roekaerts, D. and Beishuizen, N. (2012) Modeling of turbulent dilute spray combustion. *Progress in Energy and Combustion Science*, **38**, 846–887.
- Kolmogorov, A. N. (1941) The local structure of turbulence in incompressible viscous fluid for very large Reynolds numbers. *Doklady Akademii Nauk SSSR*, **30**, 299–303.
- (1962) A refinement of previous hypotheses concerning the local structure of turbulence in a viscous incompressible fluid at high Reynolds number. *Journal of Fluid Mechanics*, **13**, 82–85.
- Kumar, B. (2019) Private Communication.



- Kumar, B., Götzfried, P., Suresh, N., Schumacher, J. and Shaw, R. A. (2018) Scale dependence of cloud microphysical response to turbulent entrainment and mixing. *Journal of Advances in Modeling Earth Systems*, **10**, 2777–2785.
- Kumar, B., Janetzko, F., Schumacher, J. and Shaw, R. A. (2012) Extreme responses of a coupled scalar–particle system during turbulent mixing. *New J. Phys.*, **14**, 115020.
- Kumar, B., Schumacher, J. and Shaw, R. A. (2013) Cloud microphysical effects of turbulent mixing and entrainment. *Theor. Comp. Fluid Dyn.*, **27**, 361–376.
- (2014) Lagrangian mixing dynamics at the cloudy–clear air interface. *Journal of the Atmospheric Sciences*, **71**, 2564–2580.
- Lamb, D. and Verlinde, J. (2011) *Physics and Chemistry of Clouds*. Cambridge University Press.
- Lanotte, A. S., Seminara, A. and Toschi, F. (2009) Cloud droplet growth by condensation in homogeneous isotropic turbulence. *Journal of the Atmospheric Sciences*, **66**, 1685–1697.
- Lehmann, K., Siebert, H. and Shaw, R. A. (2009) Homogeneous and inhomogeneous mixing in cumulus clouds: Dependence on local turbulence structure. *Journal of the Atmospheric Sciences*, **66**, 3641–3659.
- Perrin, V. E. and Jonker, H. J. J. (2015) Lagrangian droplet dynamics in the subsiding shell of a cloud using direct numerical simulations. *Journal of the Atmospheric Sciences*, **72**, 4015–4028.
- Pinsky, M. and Khain, A. (2018) Theoretical analysis of mixing in liquid clouds – Part IV: DSD evolution and mixing diagrams. *Atmos. Chem. Phys.*, **18**, 3659–3676.
- Pope, S. B. (1985) PDF methods for turbulent reactive flows. *Progress in Energy and Combustion Science*, **11**, 119–192.
- (2000) *Turbulent Flows*. Cambridge University Press.
- (2011) Simple models of turbulent flows. *Physics of Fluids*, **23**, 1–20.
- Pope, S. B. and Chen, Y. L. (1990) The velocity-dissipation probability density function model for turbulent flows. *Physics of Fluids*, **2**, 1437–1449.
- Rade, L. and Westergren, B. (2013) *Mathematics Handbook for Science and Engineering*. Springer Science & Business Media.
- Rogers, R. R. and Yau, M. K. (1989) *A Short Course in Cloud Physics*. Pergamon Press.
- Sardina, G., Picano, F., Brandt, L. and Caballero, R. (2015) Continuous growth of droplet size variance due to condensation in turbulent clouds. *Physical Review Letters*, **115**, 184501.
- Siems, S. T., Bretherton, C. S., Baker, M. B., Shy, S. and Breidenthal, R. E. (1990) Buoyancy reversal and cloud-top entrainment instability. *Quarterly Journal of the Royal Meteorological Society*, **116**, 705–739.
- Siewert, C., Bec, J. and Krstulovic, G. (2017) Statistical steady state in turbulent droplet condensation. *Journal of Fluid Mechanics*, **810**, 254–280.
- Stöllinger, M., Naud, B., Roekaerts, D., Beishuizen, N. and Heinz, S. (2013) PDF modeling and simulations of pulverized coal combustion–Part 1: Theory and modeling. *Combustion and Flame*, **160**, 384–395.
- Vaillancourt, P. A. and Yau, M. K. (2000) Review of particle–turbulence interactions and consequences for cloud physics. *Bulletin of the American Meteorological Society*, **81**, 285–298.
- Vaillancourt, P. A., Yau, M. K., Bartello, P. and Grabowski, W. W. (2002) Microscopic approach to cloud droplet growth by condensation. Part II: Turbulence, clustering, and condensational growth. *Journal of the Atmospheric Sciences*, **59**, 3421–3435.
- Vaillancourt, P. A., Yau, M. K. and Grabowski, W. W. (2001) Microscopic approach to cloud droplet growth by condensation. Part I: Model description and results without turbulence. *Journal of the Atmospheric Sciences*, **58**, 1945–1964.